Supplementary Information (SI) for Journal of Materials Chemistry A.

Supporting Information

for

A soft molecular single-source precursor approach to synthesize a nanostructured Co_9S_8 (pre)catalyst for efficient water oxidation and biomass valorization

*Basundhara Dasgupta, Suptish Ghosh, Carsten Walter, Markus S. Budde, Georg J. Marquardt, Han-Hsu Chen, Markus G. M. Breithaupt, Tolga Yilmaz, Christoph Garmatter, Tamanna Ahamed, Ingo Zebger, Matthias Driess, Prashanth W. Menezes**

B. Dasgupta, S. Ghosh, C. Walter, M. S. Budde, G. J. Marquardt, H. Chen, M. G. M. Breithaupt, T. Yilmaz, C. Garmatter, Prof. Dr. M. Driess and Dr. P. W. Menezes

Department of Chemistry: Metalorganics and Inorganic Materials,

Technische Universität Berlin,

Straße des 17 Juni 135, Sekr. C2, 10623 Berlin, Germany.

*E-mail: prashanth.menezes@mailbox.tu-berlin.de

T. Ahamad, Dr. I. Zebger

Department of Chemistry: Biophysical Chemistry,

Technische Universität Berlin,

Straße des 17 Juni 115, Secr. PC14 10623 Berlin, Germany.

Dr. P. W. Menezes

Materials Chemistry Group for Thin Film Catalysis – CatLab,

Helmholtz-Zentrum Berlin für Materialien und Energie,

Albert-Einstein-Str. 15, 12489 Berlin, Germany.

*E-mail: prashanth.menezes@helmholtz-berlin.de

Table of Contents

Chemicals and Materials

All materials were used as received, without any further purification. 2-mercaptopyridine, $Co(OTf)_2$, oleylamine (70%), thiourea, $Co(NO_3)_3\cdot 6H_2O$, IrO_2 and RuO_2, and furfural were purchased from Sigma-Aldrich. 1 M aqueous potassium hydroxide (KOH; Fe < 0.05 ppm by ICP-OES), $Co(CH_3CO_2)_2\cdot 4H_2O$ and ethylenediamine was purchased from Thermo Fischer Scientific. $NaBH_4$ was purchased from Tokyo Chemical Industries. Glycerol was purchased from Honeywell Riedel-de Haën. The electrode substrate nickel foam (NF) and fluorine-doped tin oxide (FTO, resistivity 8−12 Ω/sq) were obtained from Recemat BV and Sigma Aldrich, respectively.

Characterization Details

Powder X-ray diffraction (pXRD). The powder samples were measured with a Panalytical X'Pert PRO diffractometer in Bragg-Brentano geometry with Cu-Kα radiation. The as-deposited film on FTO was measured using Panalytical X'Pert PRO MPD (multi-purpose diffractometer) for thin film analysis using grazing incidence geometry.

Single-crystal X-ray diffraction (scXRD). The crystal was mounted on a glass capillary in per-fluorinated oil and measured in a cold N_2 flow. The data of compound $[Co(PyHS)_4](OTf)_2$ was collected on an Oxford Diffraction Supernova, Single source at offset, Atlas at 150 K (Cu-*K*α-radiation, $\lambda = 1.5418$ Å). The structures were solved by direct methods with the program SHELXT[1] and refined with Olex2.[2]

Nuclear magnetic resonance (NMR). ^1H, ^{13}C, and ^{19}F NMR were recorded on a Bruker AV 500 Spectrometer and the spectra were referenced to the residual solvent signals.

Electrospray ionization mass spectroscopy (ESI-MS). ESI-MS was carried out on an Orbitrap LTQ XL of Thermo Scientific mass spectrometer, and the raw data was evaluated using the X-Calibur computer program.

Inductively coupled plasma optical emission spectroscopy (ICP-OES). ICP-OES measurements were performed on a Varian ICP-OES 715 ES. Five reference samples with elements of interest in a range between 1 to 50 ppm were used to calibrate before the measurement. The samples and references were dissolved in diluted aqua regia.

Scanning electron microscopy (SEM). SEM measurements were performed at the Zentrum für Elektronenmikroskopie (ZELMI) of the TU Berlin with a GeminiSEM500 NanoVP microscope (ZEISS) with integrated energy dispersive X-ray (EDX) detector (Bruker Quantax XFlash® 6|60). The data handling and analyses were done with the EDAX software package. The SEM EDX and elemental mapping were collected with the backscattered electron detector under a high acceleration voltage (15 KV) in order to avoid charging and fast electron collection in the detector.

Transmission electron microscopy (TEM). The TEM experiments were performed at the Zentrum für Elektronenmikroskopie (ZELMI) of the TU Berlin with a FEI Tecnai G2 20 S-TWIN transmission electron microscope (FEI Company, OR, USA) equipped with a LaB6 source at 200 kV acceleration voltage. The samples on FTO were scratched off the electrode and sonicated in acetone. Afterward, they were transferred onto a carbon-coated copper grid for investigation.

Fourier-transform infrared spectroscopy (FT-IR). FT-IR was examined using a BIORAD FTS 6000 FT-IR spectrometer under attenuated total reflection (ATR) conditions. The data were recorded in the range of 500–4000 cm^{-1} with an average of 32 scans at 4 cm^{-1} resolution.

X-ray photoelectron spectroscopy (XPS). The XPS measurements were carried out on a Kratos Axis Ultra X-ray photoelectron spectrometer (Kratos Analytical Ltd., Manchester, U.K.) using an Al Kα monochromatic radiation source (1486.7 eV) with 90° takeoff angle (normal to analyzer). The vacuum pressure in the analyzing chamber was kept at $2 \times 10-9$ Torr. The XPS spectra were collected for Co 2p, S 2p, and O 1s levels with pass energy 20 eV and step 0.1 eV. Data analyses were carried out using Casa XPS (Casa Software Ltd.) and the Vision data processing program (Kratos Analytical Ltd.).

Raman spectroscopy. Quasi *in situ* Raman spectra were recorded using the 407 nm emission of a Krypton ion laser (Innova 70, Coherent) for excitation and a confocal Raman spectrometer (Lab Ram HR- 800 Jobin Yvon) equipped with a liquid-nitrogen cooled charge-coupled device (CCD) camera for data acquisition. The typical laser power at the sample was 1 mW. One spectrum was recorded through three 240 s measurements at one location. Measurements were performed using a Linkam Cryostage THMS600 cryostat. The temperature of the films was kept at 80 K throughout the measurements. The measurements were conducted at three different parts of the film and were consistent with the attained peak positions. For the quasi *in situ* experiments, first, the chronopotentiometry (CP) was carried out at 10 mA/cm^2 (in 1 M KOH, RT) for 24 hours and thereafter freeze-quenched at 1.56 V_{RHE}. The CA measurements were performed for 10 minutes until a stable current was obtained and the films were then freeze-quenched using liquid N_2 under continuous Ar gas flow and stored in liquid N_2 until measurement.

Synthesis of [Co(PyHS)$_4$](OTf)$_2$ (1)

2-mercaptopyridine (0.934 mg, 8.4 mmol, 8.4 equiv.) and Co(OTf)$_2$ (0.357 g, 2.0 mmol, 2.0 equiv.) were weighed into a 50 mL Schlenk tube equipped with a stir bar. To this, 20 mL of dichloromethane was added, and the reaction mixture was stirred for 16 hours at ambient temperatures. During this time, a light green precipitate was formed. After stirring overnight, all the volatiles were removed under a vacuum. The obtained residue was washed with diethyl ether (3 × 15 mL), filtered, and dried under vacuum for two hours affording a brown-green solid with 86% yield (1.38 g, 1.72 mmol). Single crystals suitable for X-ray diffraction analysis were obtained by keeping a saturated solution of **1** in tetrahydrofuran (THF) at room temperature for one day.

^{1}H-NMR (500MHz, CD$_3$CN, paramagnetic): δ(ppm) = 12.71 (br, 4 H), 11.21 (br, 4 H), -3.24 (br, 4 H), -5.96 (br, 4 H), -11.45 (br, 4H).

^{19}F-NMR (500MHz, CD$_3$CN): δ(ppm) = –78.33.

ESI-MS (positive ion mode, THF): m/z = 538.93 [{Co(PyHS)(PyS)$_3$}+K]$^+$, 388.95 [{Co(PyS)$_3$]$^+$, 278.95 [Co(PyS)$_2$]$^+$, 221.02 [(PyS)$_2$+H]$^+$.

IR (ATR, diamond): ν(cm^{-1}) = 1375 (C–F), 1132 (S=O).

Synthesis of Co_9S_8 from Complex 1

To a three-necked round-bottom flask attached to a condenser, 15 mL oleylamine was added. The solvent was degassed by a 3-cycle freeze-pump method. The whole set-up was degassed using a vacuum followed by refilling with nitrogen three times and then the flask was heated to 260 °C. The precursor (0.500 g, 0.62 mmol) was dissolved in 5 mL of dry oleylamine at 30 °C in another Schlenk flask. The solution was transferred to the three-necked flask at 260 °C by injection under inert conditions. The reaction temperature was maintained at 260 °C for 3 hours and then the mixture was allowed to cool down to room temperature. The whole reaction mixture was transferred into a centrifuge tube and centrifuged along with an additional 20 mL ethanol at 9000 rpm to produce a black solid. Washing with ethanol was repeated thrice to remove any excess ligands and oleylamine. The precipitate was then washed with acetone, dried at 60 °C overnight in air, and stored for further use.

Synthesis of CoS from Complex 1

A similar procedure as mentioned above was adopted for the synthesis of CoS from precursor **1**, except that the temperature of the reaction was set to 225 ^{o}C.

Synthesis of $Co(OH)_2$.

1 mmol of $Co(NO_3)_2.6H_2O$ was dissolved in 10 mL of deionized water at room temperature, and to this, 15 mL of KOH (0.1 M) was added dropwise, with stirring. The stirring was then continued for another 30 min. A pink solid product appeared as a precipitate, which was separated by centrifugation, washed with deionized water (3 × 50 ml), and dried at 60 °C overnight in air to obtain $Co(OH)_2$.

Synthesis of CoOOH.

The as-prepared $Co(OH)_2$ was dispersed in 20 mL of deionized water, which was then heated slowly up to 80 °C. An excess of $K_2S_2O_8$ was added with stirring and the same temperature and stirring conditions were maintained for another 1 h until a complete change of colour to brown was observed. The precipitate was separated by centrifugation, washed with deionized water (3 × 50 ml), and dried at 60 °C overnight in air to obtain CoOOH.

Synthesis of Co_3O_4.

The as-prepared $Co(OH)_2$ was calcined in air at 350 ^{o}C for 2 hours to obtain Co_3O_4.

Synthesis of Co_9S_8 via hydrothermal approach

Into a 15 ml aqueous solution of 0.348 g of $Co(CH_3COO)_2{\cdot}4H_2O$ and 0.076 g of thiourea, 0.08 g of $NaBH_4$ and 10 ml of ethanol was added. After vigorously stirring for 30 min, the mixture was transferred into a 50 ml Teflon-lined autoclave and kept at 175 °C for 12 hours. After cooling down to room temperature, the precipitate was separated by centrifugation, washed with deionized water and absolute ethanol, and dried at 60 °C overnight in air.

Electrophoretic deposition (EPD)

The powder samples were deposited on NF and FTO using a chemical binder-free electrophoretic method by applying a potential difference of 10 V in a mixture of iodine (I_2) and acetone. The EPD area was fixed to a 1 × 1 cm^2 area. The distance between two electrodes during the EPD process was kept at 1 cm. For the typical deposition protocol, 20 mg of the catalyst powder was suspended in 10 ml acetone, and 3 mg of I_2 was then added. This solution was kept under ultrasonication for 1 hour. The EPD was conducted under continuous stirring at room temperature. The mass loadings were monitored carefully by recording the electrode weight before and after EPD using a KERN ABJ220-4NM microbalance (KERN GmbH, Germany). Depending upon the catalyst, the loading was optimized by varying the EPD time and the obtained loadings on NF and FTO were ~ 0.8 ± 0.1 mg/cm^2 and ~ 0.5 ± 0.1 mg/cm^2, respectively for all the catalysts. The mass loading was reproducible within the margins of an experimental error.

Electrochemical Measurements for the Oxygen Evolution Reaction (OER)

The electrochemical measurements were performed using a standard three-electrode (working, counter, and reference) setup with 40 ml 1 M aqueous KOH solution (pH 13.89)[3] and a SP-200 potentiostat from BioLogic Science Instruments controlled by the EC-Lab v10.20 software package. FTO and NF were used as the working electrode, Pt wire (0.5 mm diameter × 230 mm length, A-002234, BioLogic) as the counter, and Hg/HgO (CH Instruments, Inc.) as the reference electrode. The Hg/HgO potentials were referenced to the reversible hydrogen electrode (RHE).[4]

***iR* compensation:** The potential was corrected by 90% of the uncompensated resistance (R_u ~ 10 Ω/cm^2).

Cyclic voltammetry (CV) and linear sweep voltammertry (LSV). CVs and LSVs were measured with *iR* correction and without stirring. The potentials were measured in a 1 M aqueous KOH (pH 13.8) solution and referenced to the reversible hydrogen electrode (RHE) through calibration. The potential was calculated with the following equation: $E(RHE) = E(Hg/HgO) + 0.098\ V + (0.059 \times pH)\ V$

Electrochemical impedance spectroscopy (EIS). EIS was recorded at 1.56 V_{RHE} for FTO samples to obtain the Nyquist plots. The amplitude of the sinusoidal wave was examined in a frequency range of 100 kHz to 1 mHz. The curves were fitted to a Randles equivalent circuit, where R_s, CPE, and R_{ct} are the equivalent series resistance, the constant phase element of the double-layer capacitance, and the charge transfer resistance, respectively.

Chronoamperometry (CA) and chronopotentiometry (CP). The CA and CP measurements were performed with *iR* compensation (90%).

Steady-state Tafel analysis. CA measurements were performed for 3 min for each potential step to acquire the stable current densities. The Tafel equation $\eta = b \times \log(j) + a$, was applied to determine the Tafel slope. Herein, η is the overpotential (V), b is the Tafel slope (mV/dec), and j is the current density (mA/cm^2).[5]

Double-layer capacitance (C_{dl}). CVs were measured in a range where no apparent faradaic process occurred, from -0.025 to 0.025 V_{OCP} (open circuit potential), at varying scan rates between 5 and 60 mV/s. Half of the potential difference at 0.00 V_{OCP} was then plotted as a function of the scan rate. The resulting slope was used to determine the C_{dl}.

Faradaic efficiency (FE). The FE of Co_9S_8 in 1 M aqueous KOH towards OER was measured on NF in a closed two-electrode cell. The cell comprised of two burettes, which were connected using a glass pipe. Co_9S_8/NF anode was fixed in one burette while the Pt wire cathode was fixed in the other burette. A constant current density of 50 mA/cm^2 was applied for 1 h. A stoichiometric H_2 and O_2 gases were generated in the headspace of the cathode and anode burette, respectively, and resulted in a decrease in water volume in the burettes. The FE is calculated based on:

$$\text{FE } (O_2,\%) = (4 \cdot F \cdot p \cdot V_{O_2}) / (R \cdot T \cdot j \cdot t) \text{ x } 100\%$$

where F is the Faraday constant (96485 C/mol), p is the pressure (101 kPa), V_{O2} is the evolved volume of oxygen, which is equal to the amount of water volume decrease in the anode burette after CP, R is the ideal gas constant (8.314 J/mol-K), T is the temperature (298 K), j is the current density (the potentiostat was set to 50 mA/cm^2 but the real current that was measured on average by the potentiostat was only 49.3 mA/cm^2), and t is the period of electrolysis (3600 s).

Turnover Frequency (TOF). TOF was calculated according to the following equation:

$$\text{TOF} = (j \cdot A) / (z \cdot F \cdot m)$$

where j is the OER current density (achieved from the steady state polarisation curve with a slow scan rate of 5 mV/s at 1.63 V_{RHE}, which minimized the influence of the current from the metal redox, and the capacitance), A is the geometrical surface area of the electrode (1 cm^2), z is the unitless number of electrons needed to form O_2 (4), F is the faradaic constant (96485 C/mol), and m is the number of redox active Co sites, which were calculated based on the equations of Figure S18 and under the assumption that 2 electrons per active cobalt site were transferred during the redox process.

Electrochemical Measurements for Organic Oxidation Reactions (OOR)

Electrolysis of organic substrates. The LSV and bulk electrolysis measurements were conducted in a three-electrode setup in analogy to the one used for OER tests, with 15 mL KOH and 0.1 M glycerol or furfural. Co_9S_8/NF and bare NF were used as the anode, platinum wire as the cathode, and Hg/HgO as the reference electrode. The LSV was performed without stirring. The bulk electrolysis was investigated using the CA technique at different potentials of 1.35, 1.40, 1.46, and 1.50 V_{RHE}, with stirring at 300 rpm.

Reusability test. For the reusability test of glycerol oxidation with Co_9S_8/NF, a fresh solution of 10 mM glycerol in 15 mL of 1 M KOH was taken for each cycle and CAs were measured at 1.46 V_{RHE}, with 300 rpm stirring, until the charge required for full conversion (115.8 C) was passed in each cycle.

Hybrid water electrolysis (HWE). The HWE was conducted in a divided cell with a 2-electrode set-up, wherein the anodic and cathodic chambers were separated by an anion exchange membrane. The oxidation of glycerol and furfural with Co_9S_8/NF in the anodic half-cell was coupled with hydrogen evolution reaction (HER) with Pt wire in the cathodic half-cell. Electrochemical measurements were conducted with 0.1 M glycerol/ furfural in 15 mL of 1 M KOH in the anodic half-cell and pure 1 M KOH in the cathodic half-cell. The bulk electrolysis was investigated using the CA technique at a cell potential of 1.60 V, with stirring at 300 rpm in the anodic chamber.

NMR Analysis. The oxidation reaction solutions were characterized using ^1H and ^{13}C NMR spectroscopy. The NMR sample was prepared by mixing a 150 µL aliquot of the reaction solution, 0.1 M maleic acid (internal standard), and 450 µL D_2O solvent. MestReNova software was used to process and plot the spectra. At 4.7 ppm, a sharp peak can be observed, which represents the H_2O from the aqueous reaction mixture. This peak was also used as a reference to reflect the chemical shifts of the other proton signals.

Calculation of FE. The FE for organic oxidation was calculated based on the moles of formed products and the associated passed charge. The product identification and conversion were determined by ^1H NMR spectroscopy using maleic acid as the internal standard of known concentrations. The FE of product formation was calculated using the following equation:

$$\text{FE (\%)} = (\text{mol of product formed} \cdot F \cdot n_e) / (\text{total charge passed}) \times 100\%$$

where F is the Faraday constant (96485 C/mol), n_e is the number of electrons required for the oxidation process, which is 8 for glycerol oxidation, and 2 for furfural oxidation.

Calculation of Yield Rate. The production or yield rate of the organic oxidation products was calculated using the following equation:

$$\text{Yield Rate of the product} = \text{mmol}_{\text{product}} / (\text{mmol}_{\text{substrate}} \cdot A \cdot t)$$

where $\text{mmol}_{\text{product}} = (\text{Product}_{\text{yield}} \cdot \text{mmol}_{\text{substrate}})/100$, A is the surface area of the electrode, and t is the electrolysis time (h). The yield rate of H_2 in HWE was calculated as $\text{mmol}_{H_2}\ h^{-1}\ cm^{-2}$.

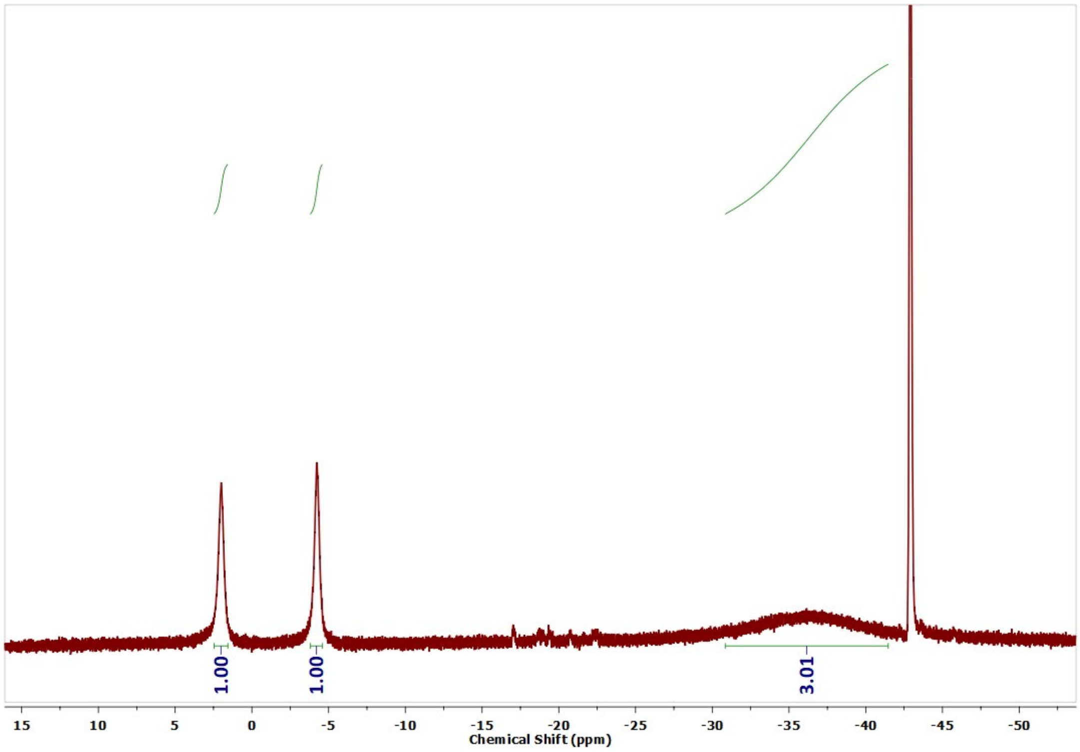

Figure S1. ^{1}H NMR spectrum of 1(OTf)$_2$ in CD$_3$CN at 500 MHz.

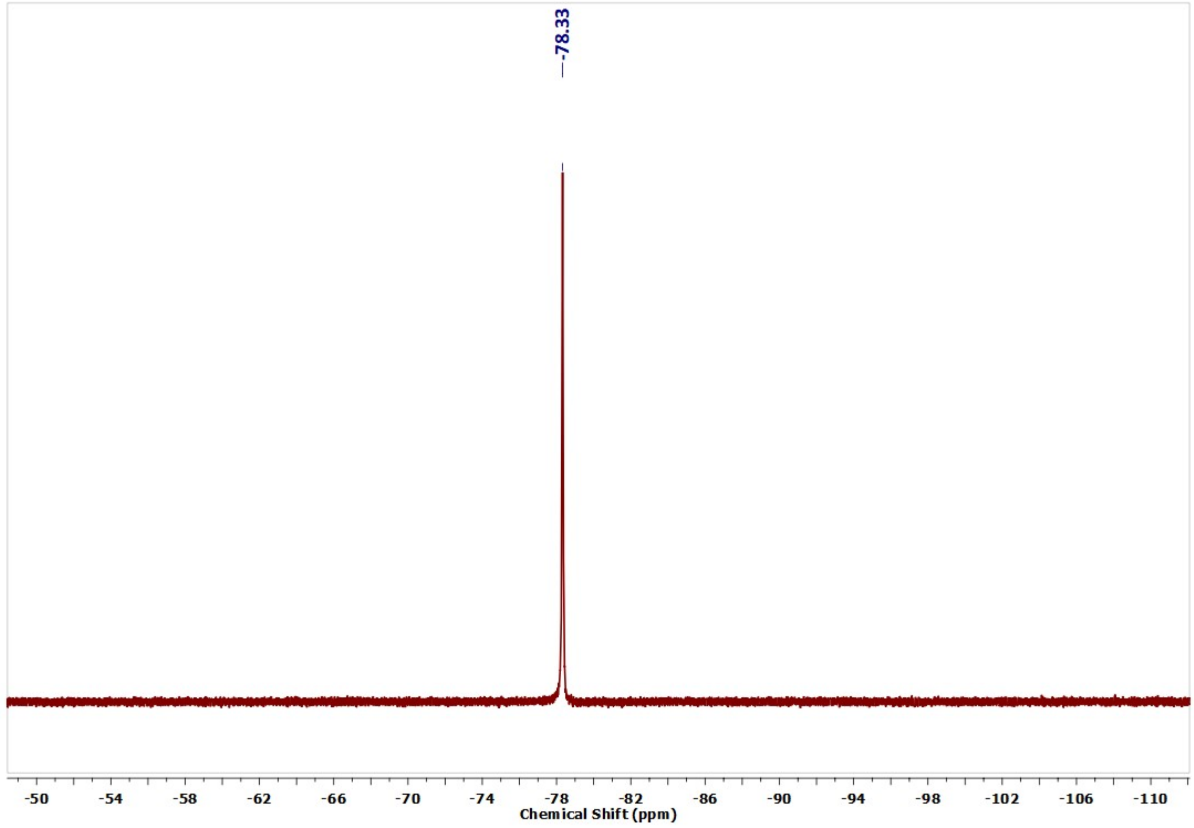

Figure S2. ^{19}F NMR spectrums of 1(OTf)$_2$ in CD$_3$CN at 500 MHz.

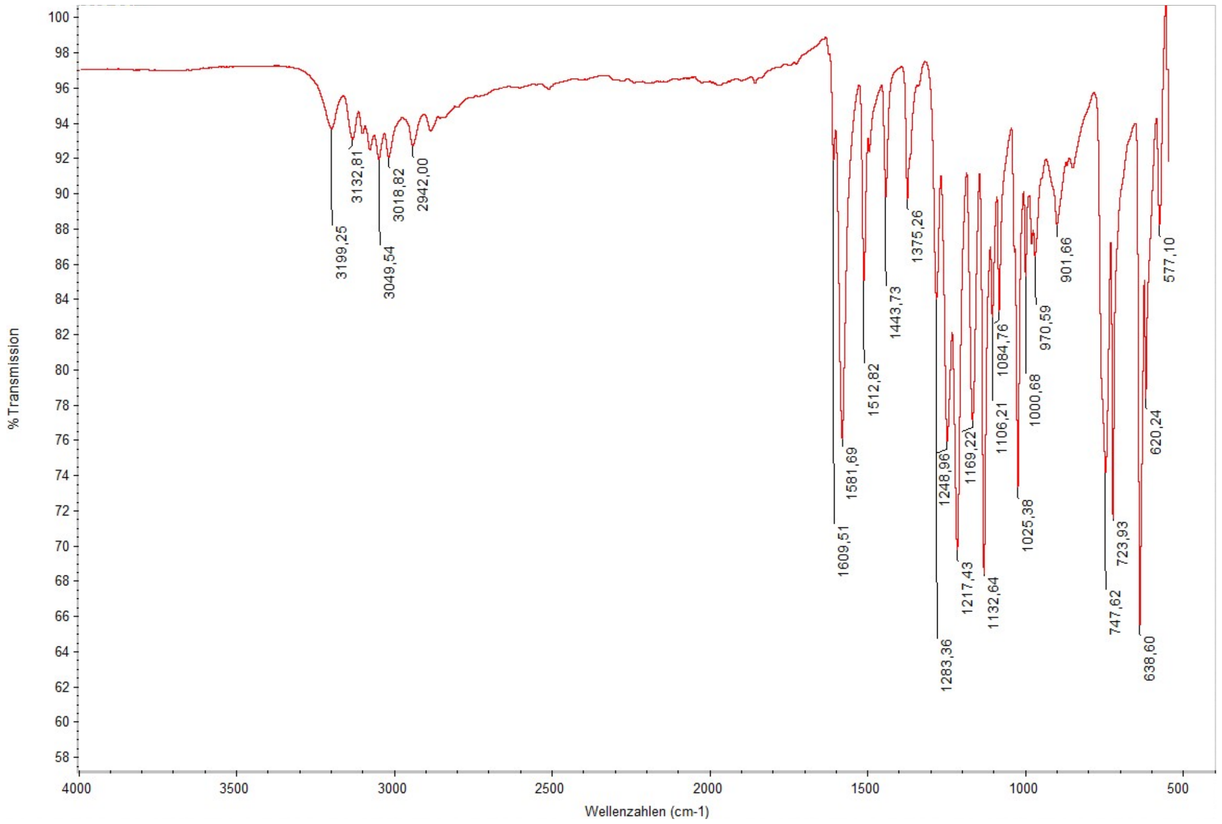

Figure S3. FT-IR spectrum of 1, two strong vibrations at 1132 and 1375 cm^{-1} can be assigned to the vibrations of *v*(S=O) and *v*(C–F), respectively, of the triflate counter anion.

Table S1. Crystal data and structure refinement for complex **1** (CCDC file number 2338752).

Empirical formula	C42 H60 Co F6 N4 O11 S6
Formula weight	1162.23
Temperature	150.0 K
Wavelength	1.54184 Å
Crystal system	Monoclinic
Space group	*P* 1 21/*c* 1
Unit cell dimensions	a = 12.3474(3) Å, α = 90° b = 21.6983(8) Å, β = 95.219(3)° c = 20.6085(6) Å, γ = 90°
Volume	5498.5(3) Å^3
Z	4
Density (calculated)	1.404 Mg/m^3
Absorption coefficient	5.242 mm^{-1}
F(000)	2420
Crystal size	0.28 x 0.21 x 0.12 mm^3
Theta range for data collection	2.964 to 72.502°
Index ranges	-14<=h<=12, -25<=k<=26, -23<=l<=25
Reflections collected	23727
Independent reflections	10635 [R(int) = 0.0732]
Completeness to theta = 67.684°	99.8%
Absorption correction	Semi-empirical from equivalents
Max. and min. transmission	1.00000 and 0.17587
Refinement method	Full-matrix least-squares on F^2
Data / restraints / parameters	10635 / 74 / 631
Goodness-of-fit on F^2	1.016
Final R indices [I>2sigma(I)]	R_1 = 0.0645, wR_2 = 0.1506
R indices (all data)	R_1 = 0.1163, wR_2 = 0.1853
Extinction coefficient	n/a
Largest diff. peak and hole	0.701 and -0.386 e.Å^{-3}

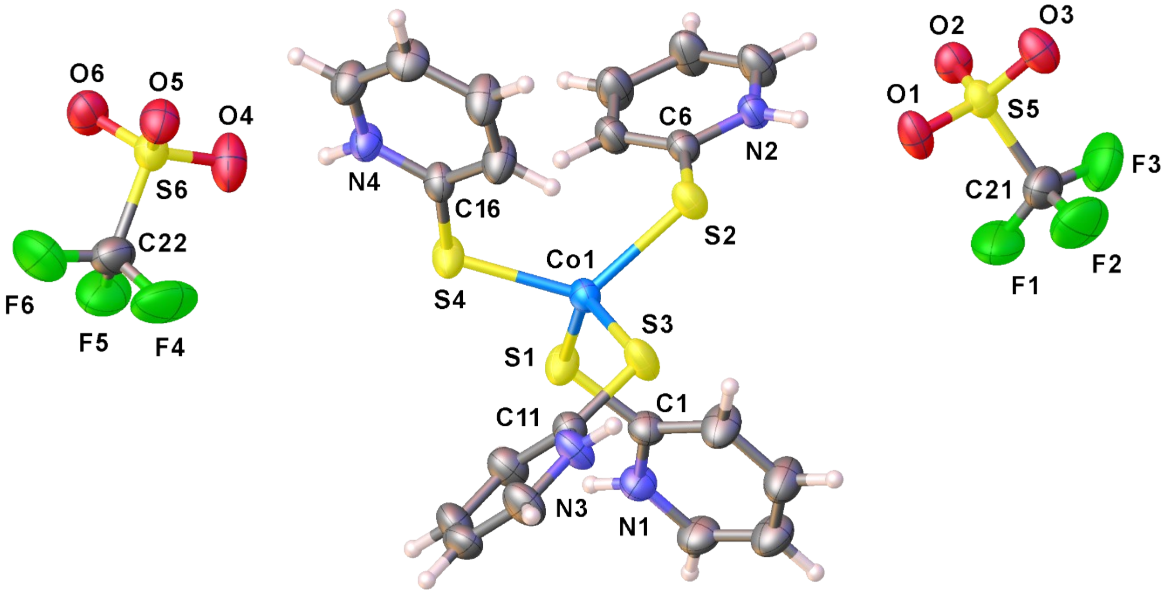

Figure S4. Molecular structure of **1**. The molecular structure has been depicted with thermal ellipsoids at 50% probability. Color code; cobalt: blue, sulfide: yellow, carbon: gray, nitrogen: purple, oxygen: red, and fluorine: green. The crystal structure of **1** also contains 5 additional THF solvent molecules coordinated with it, which have been omitted here for clarity. The entire structure is shown in the CCDC file number 2338752.

Table S2. Selected bond lengths [Å] and angles [°] for **1**.

Bond lengths [Å]		**Bond angles [°]**	
Co1-S1	2.2898(12)	S(1)-Co(1)-S(2)	116.66(5)
Co1-S2	2.2948(13)	S(1)-Co(1)-S(3)	121.83(6)
Co1-S3	2.2949(14)	S(1)-Co(1)-S(4)	91.26(5)
Co-S4	2.2987(14)	S(2)-Co(1)-S(3)	90.13(5)
S1-C1	1.730(5)	S(2)-Co(1)-S(4)	121.95(6)
S2-C6	1.727(5)	S(3)-Co(1)-S(4)	118.06(5)
S3-C11	1.727(5)	C(1)-S(1)-Co(1)	108.13(15)
S4-C16	1.727(5)	C(6)-S(2)-Co(1)	106.76(15)
N1-C1	1.345(5)	C(11)-S(3)-Co(1)	107.23(17)
N2-C6	1.350(6)	C(16)-S(4)-Co(1)	107.91(16)
N3-C11	1.348(6)	N(1)-C(1)-S(1)	116.4(4)
N4-C16	1.348(6)	N(2)-C(6)-S(2)	117.2(3)
N1-H1	0.8800	N(3)-C(11)-S(3)	116.8(3)
		N(4)-C(16)-S(4)	117.0(3)

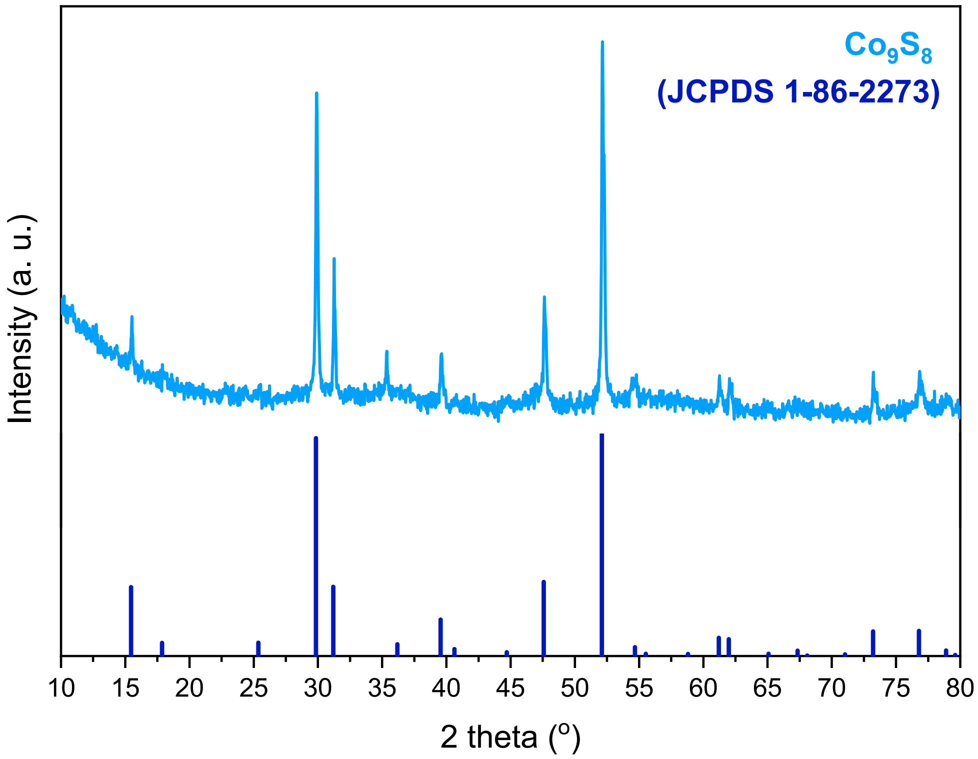

Figure S5. pXRD pattern of Co_9S_8 phase derived from complex **1**.

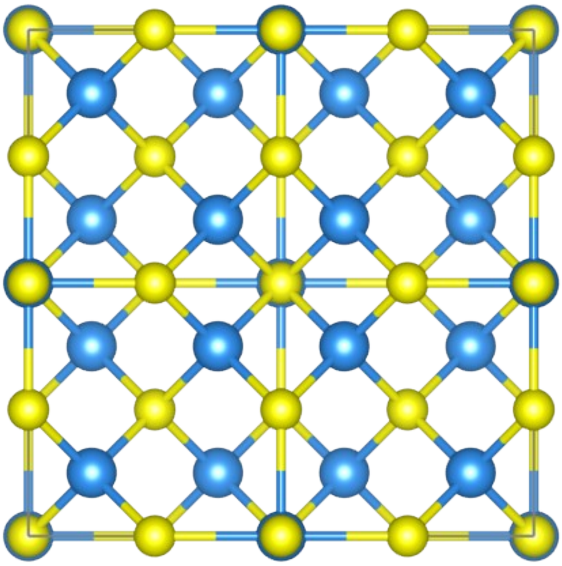

Figure S6. The crystal structure of Co_9S_8 (blue: Co, yellow: S) on the crystallographic direction [100]/ [010]/ [001].

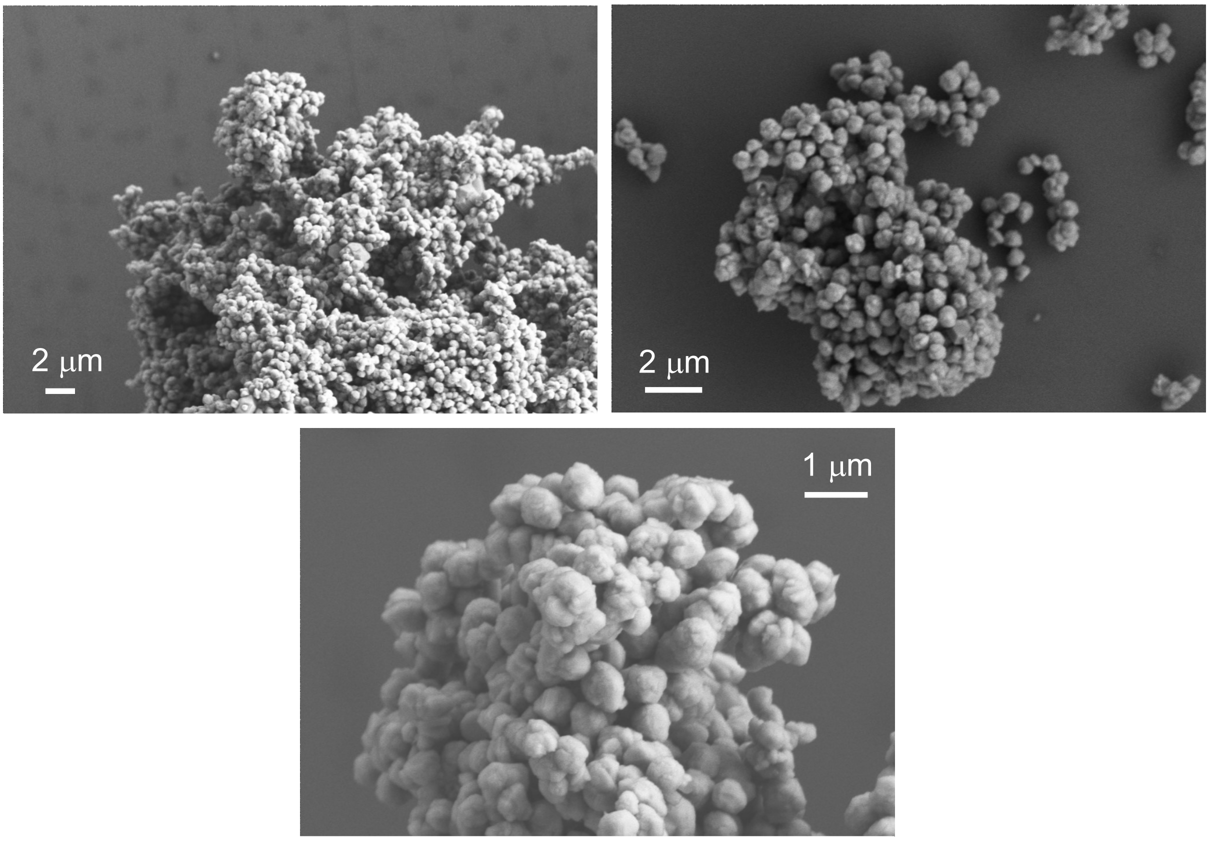

Figure S7. SEM images of Co_9S_8 at different magnifications show the presence of hexagon-like agglomerates.

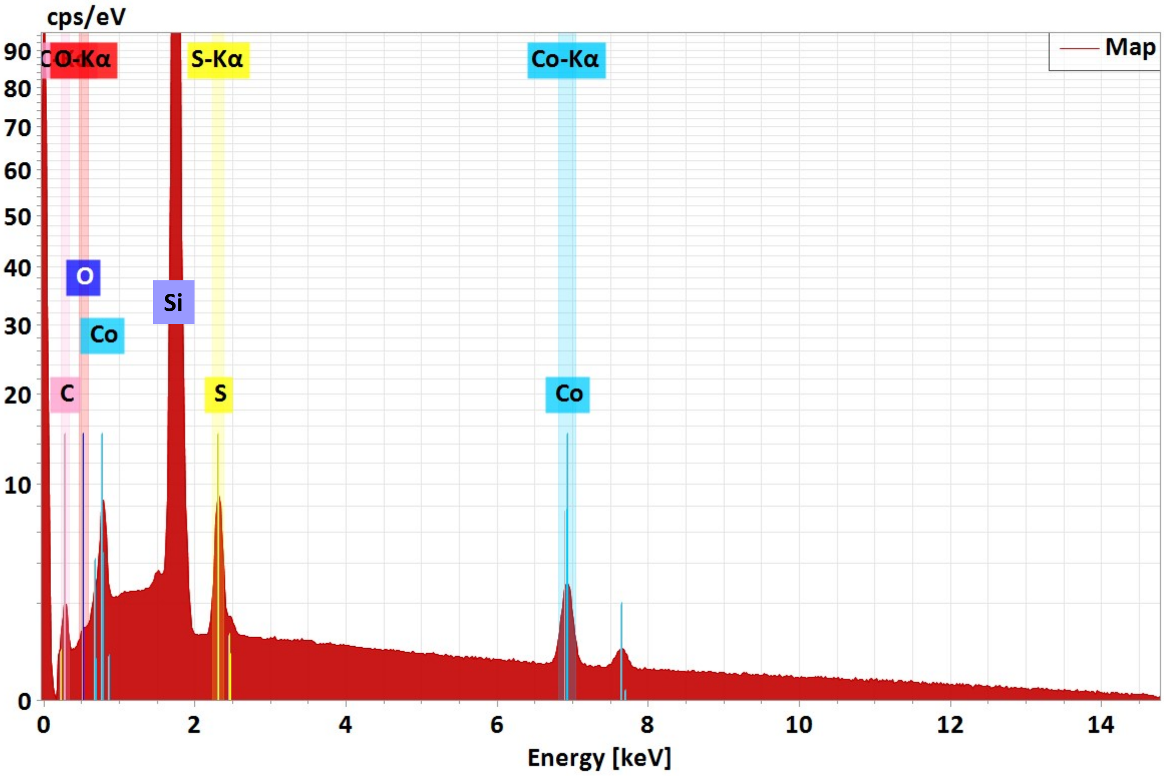

Figure S8. EDX spectrum of Co_9S_8 confirms the Co:S ratio to be 1:0.89 in the sample. The Si peak comes from the Si wafer substrate. The oxygen content is < 1%.

Table S3. Determination of Co:S ratio in Co_9S_8 under different conditions from ICP-OES and EDX.

Sample	**Co:S ratio**	
	ICP-OES	**EDX**
Co_9S_8 powder	1:0.89	1:0.89
Co_9S_8 deposited on FTO	1:0.89	1:0.88
Co_9S_8 after 24 h CP at 10 mA/cm^2	1:0.01	1:0.01

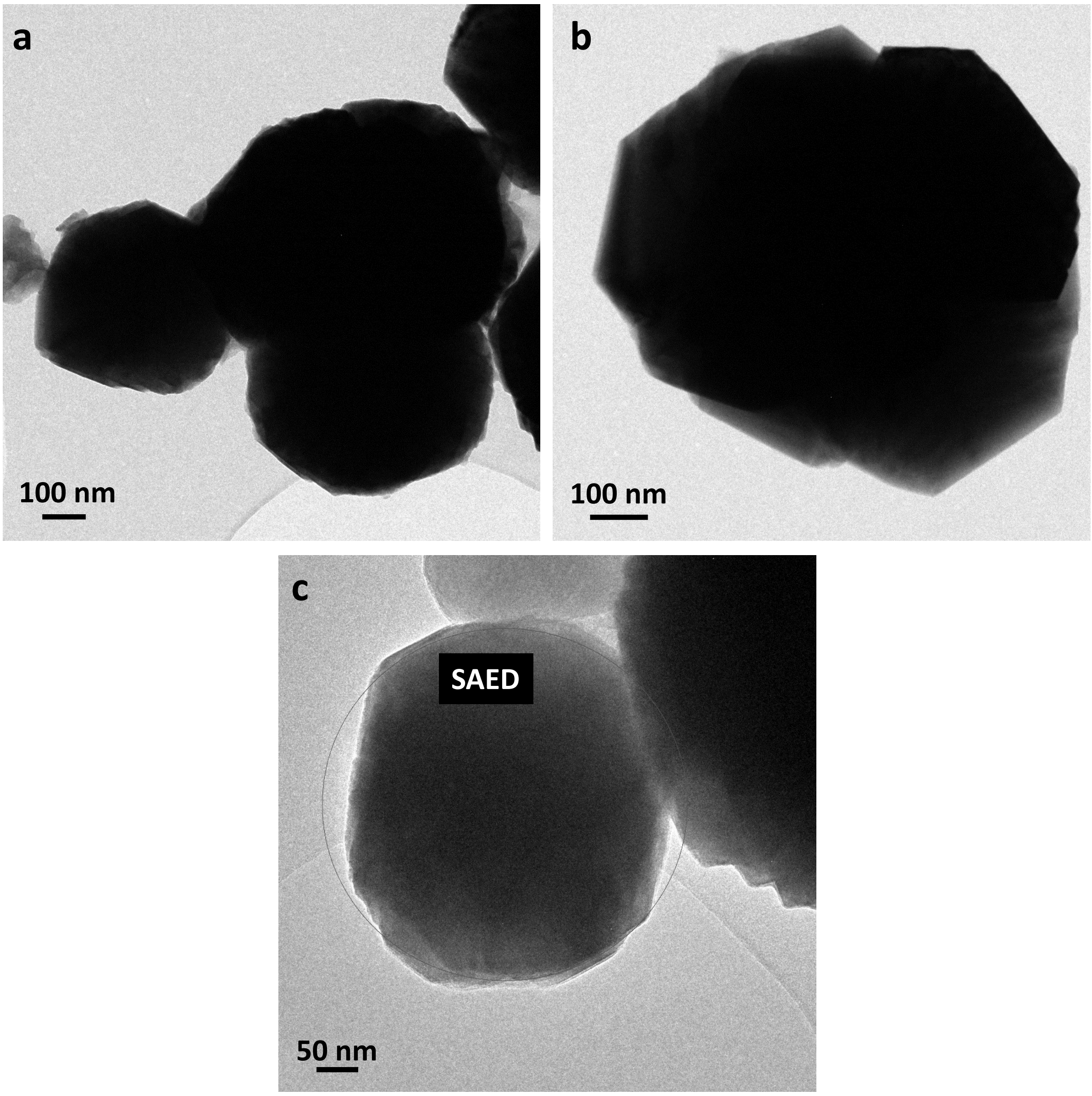

Figure S9. TEM image of Co_9S_8 at different magnifications. The images show hexagon-like particle aggregates. The corresponding SAED is shown in Figure 2d of the Manuscript.

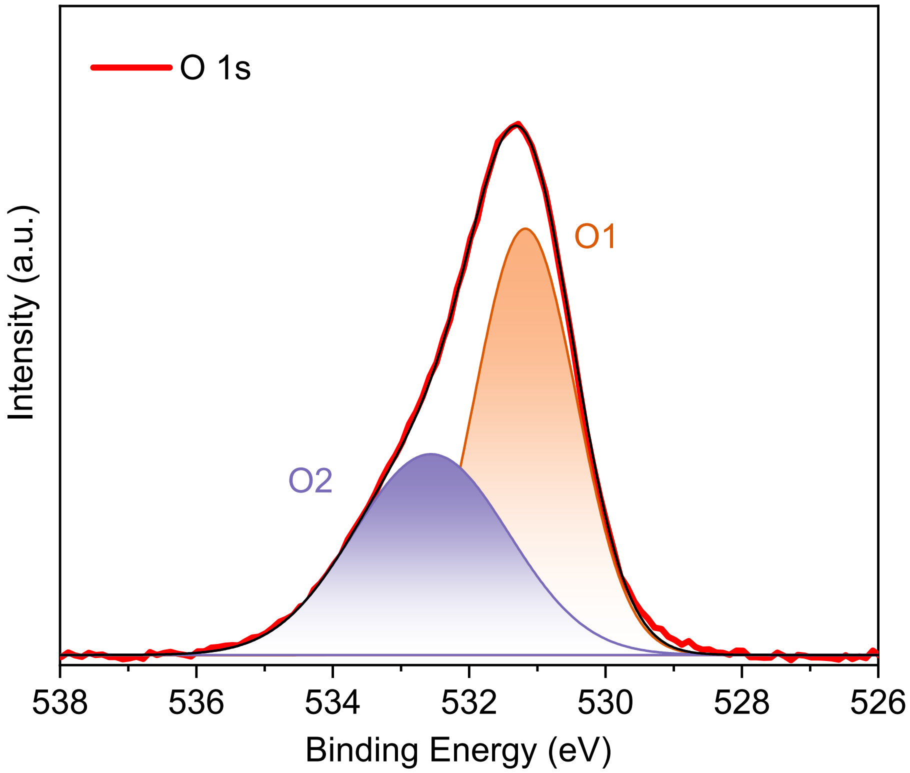

Figure S10. The deconvoluted O 1s spectrum of as-prepared Co_9S_8 shows peaks associated with oxide species (O1) and surface hydroxylation (O2) derived from air exposure.[6]

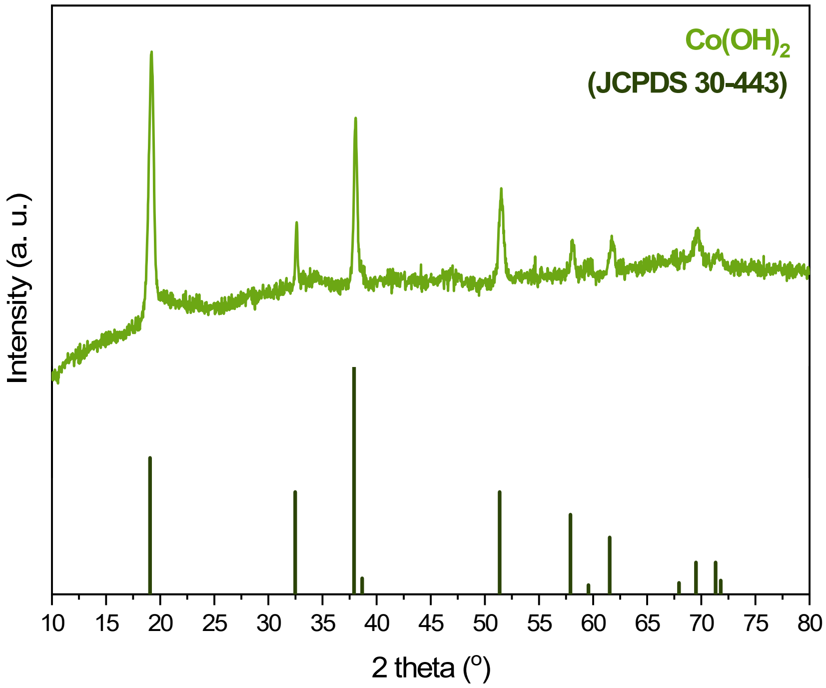

Figure S11. pXRD pattern of Co(OH)$_2$.

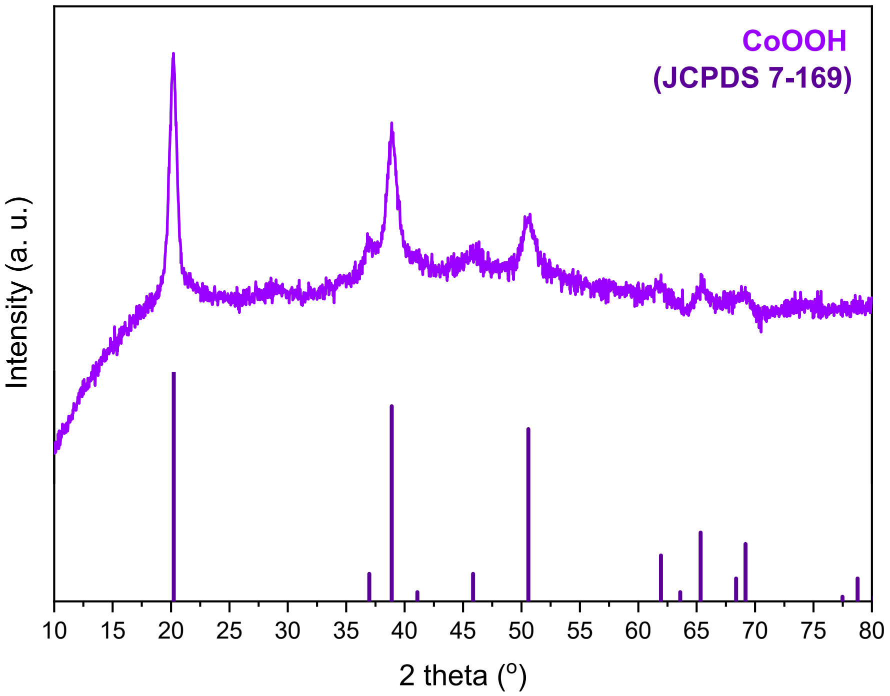

Figure S12. pXRD pattern of CoOOH.

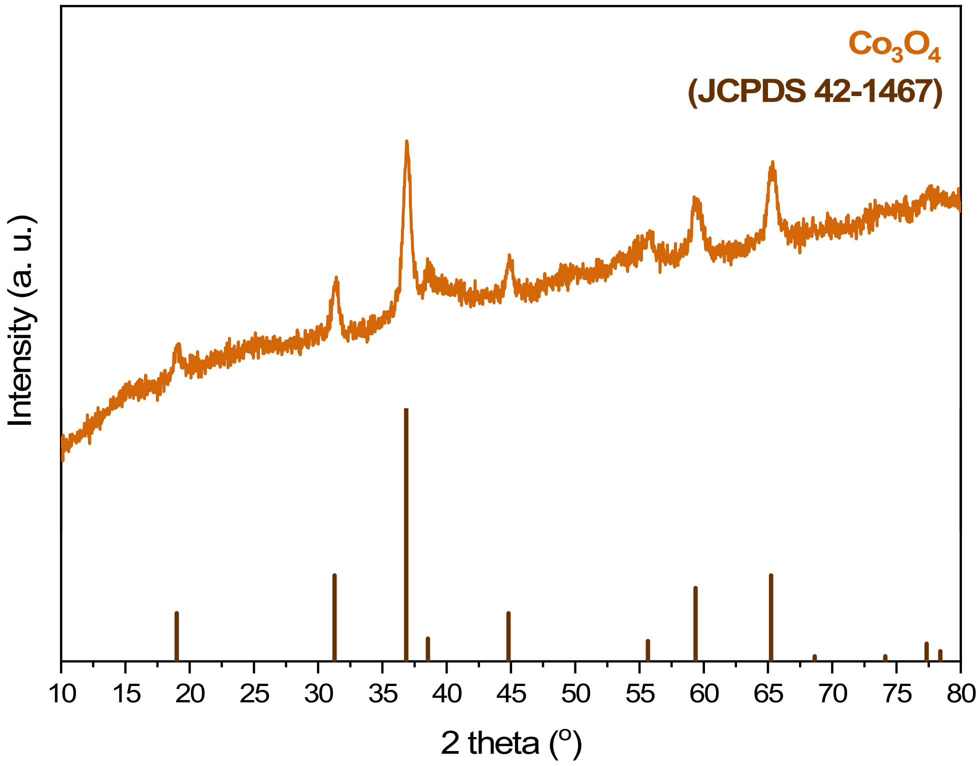

Figure S13. pXRD pattern of Co_3O_4.

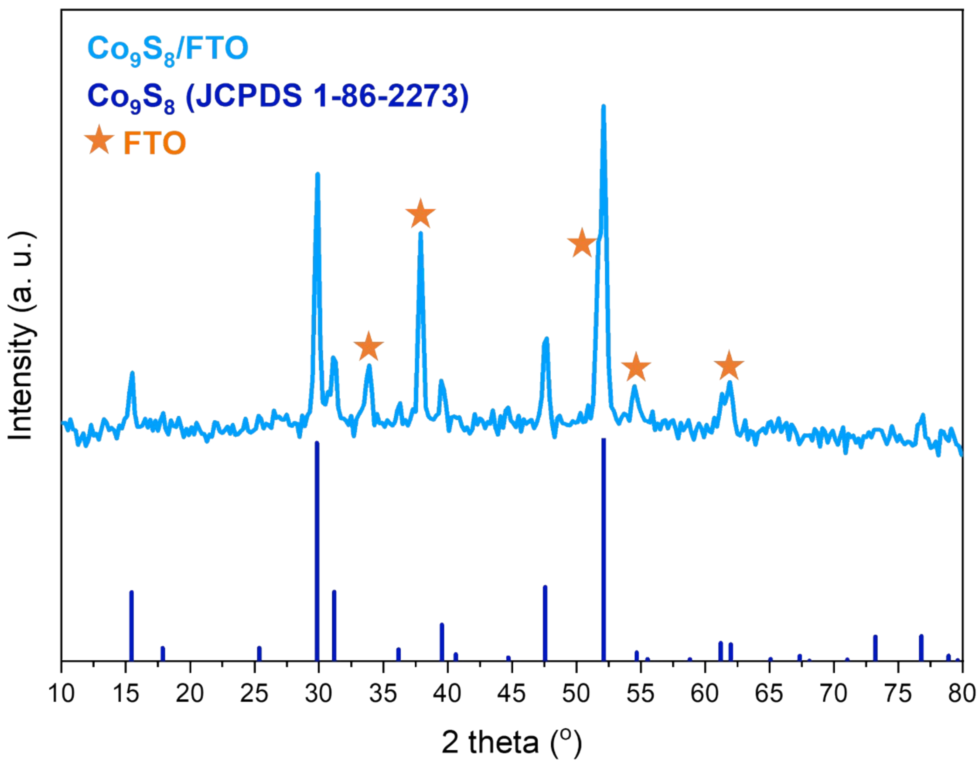

Figure S14. pXRD pattern of as-deposited Co_9S_8 film on FTO. The pattern confirms that the crystal structure of Co_9S_8 remains unchanged after EPD.

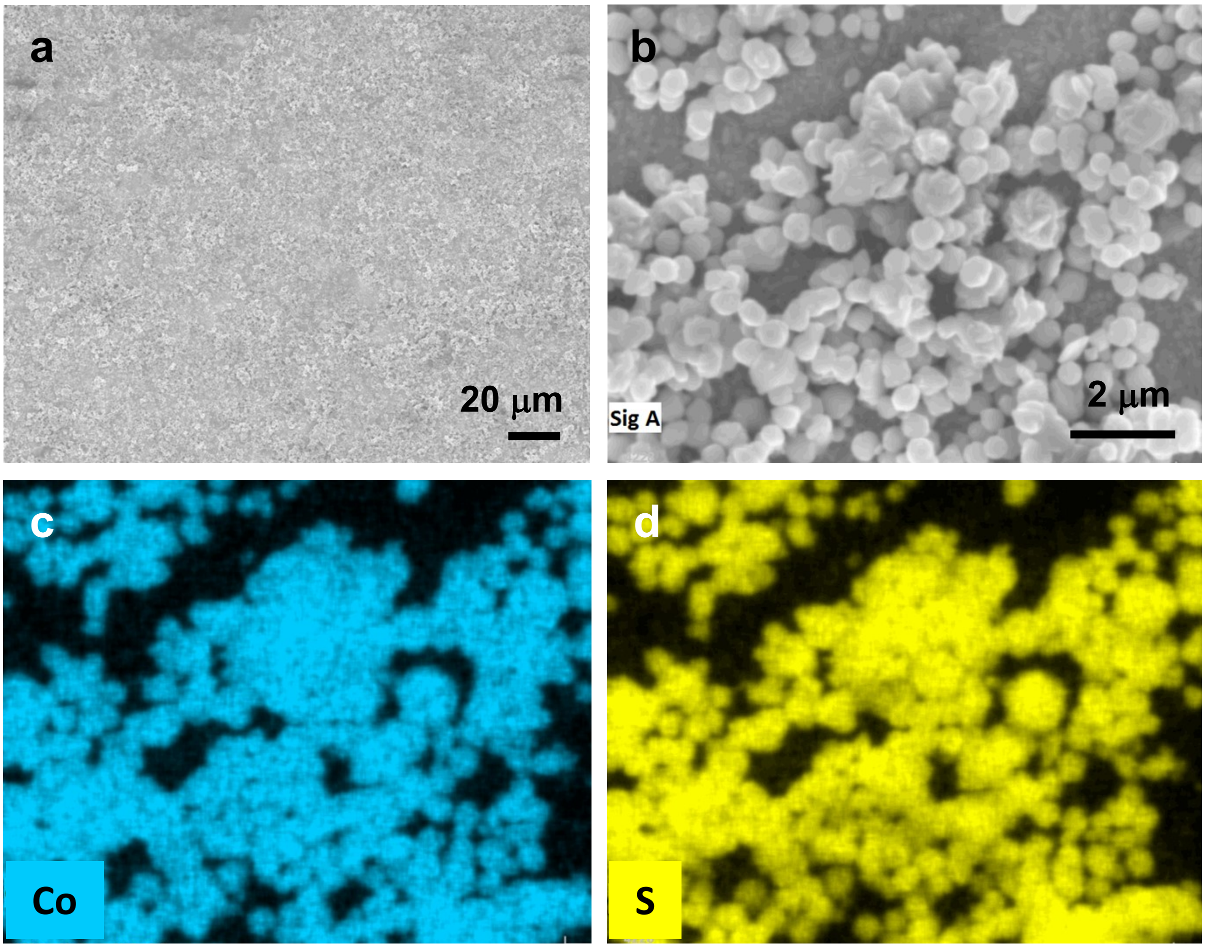

Figure S15. (a) SEM images of as-deposited Co_9S_8 film on FTO showing a homogeneous deposition of the material on the substrate. (b) SEM image of the film showing a retention of the morphology of Co_9S_8 after deposition, and the corresponding (c, d) elemental mapping shows a homogeneous distribution of Co (blue) and S (yellow) in the as-deposited sample. These results are similar to as-synthesized Co_9S_8.

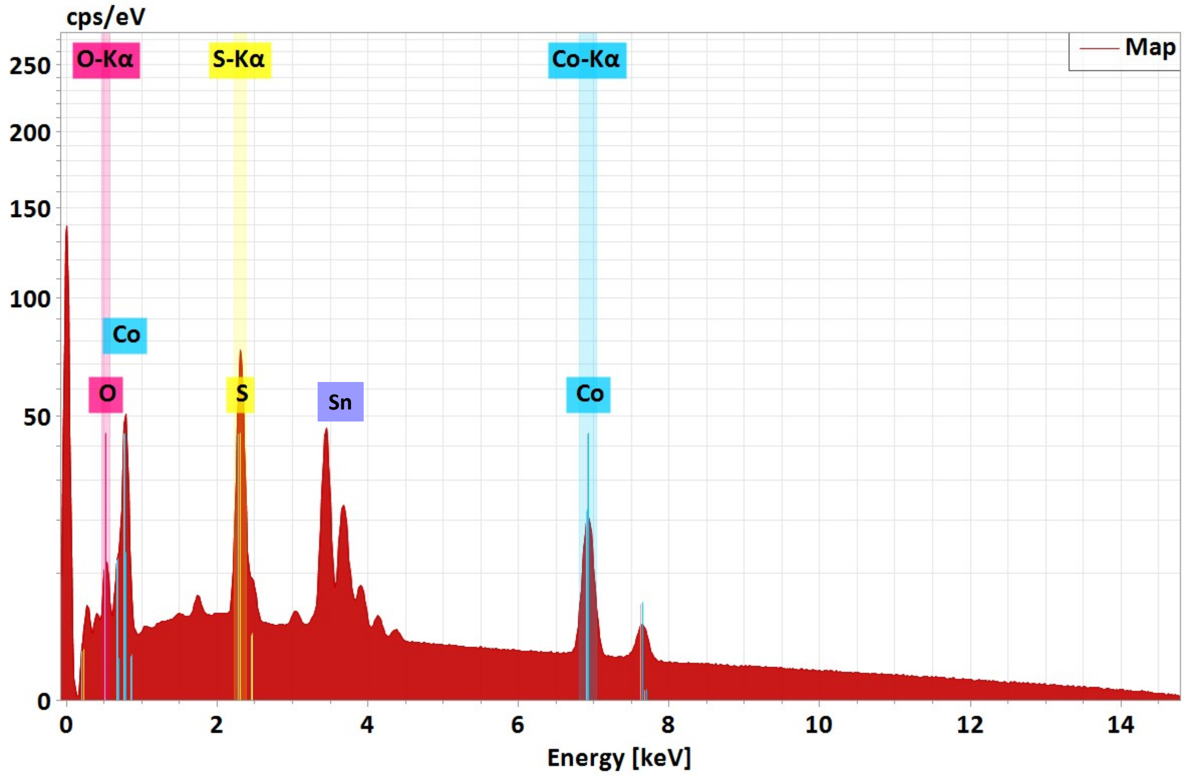

Figure S16. EDX spectrum of as-deposited Co_9S_8 film on FTO confirms the Co:S ratio to be 1:0.89 in the sample. Sn and O signals arise from the FTO glass substrate electrode. These results are similar to as-synthesized Co_9S_8.

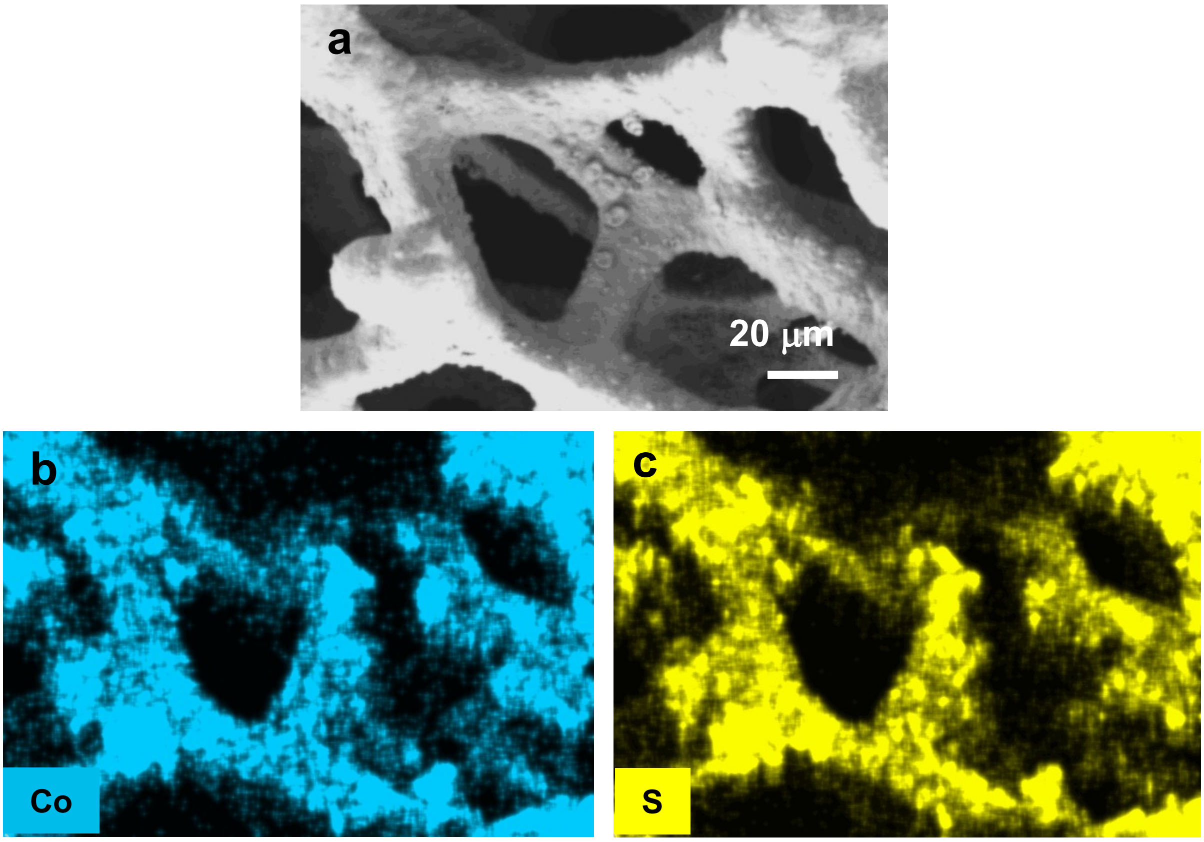

Figure S17. (a) SEM image of as-deposited Co_9S_8 film on NF showing a homogeneous deposition of the material throughout the NF substrate. (b, c) Elemental mapping shows the homogeneous distribution of Co (blue) and S (yellow) in the as-deposited sample. These results are similar to as-synthesized Co_9S_8.

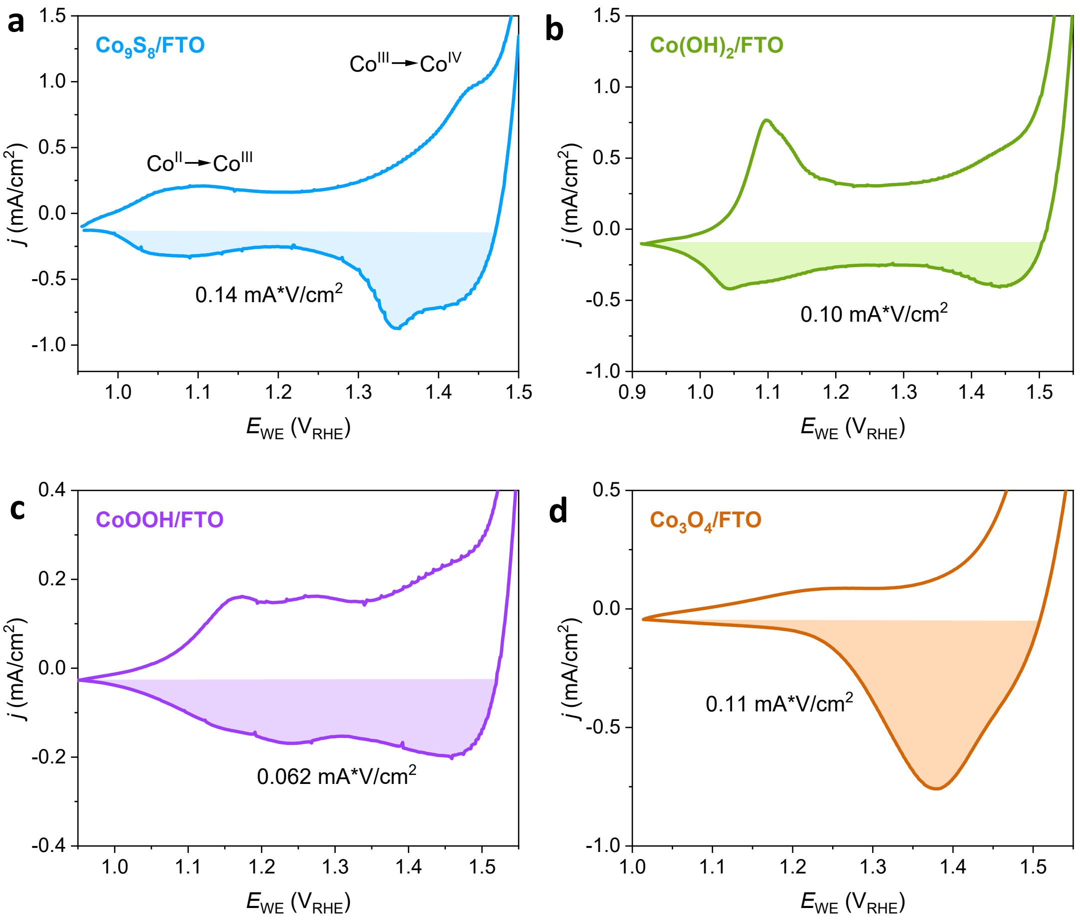

e

$$[e^-] = \frac{1}{\text{scan rate} * F} * \int_{V_1}^{V_2} I(E)dE$$

Scan rate = 5 mV/s, F = 96485 sA/mol

Material	$\int_{V_1}^{V_2} I(E)dE$ **(mA*V)**	**[e-] (µmol)**
Co_9S_8	0.14	0.29
$Co(OH)_2$	0.10	0.20
CoOOH	0.062	0.13
Co_3O_4	0.11	0.23

Figure S18. Integration of the reduction peaks (Co$^{IV/III}$ and Co$^{III/II}$) of (a) Co_9S_8/FTO, (b) $Co(OH)_2$/FTO, (c) CoOOH/FTO, and (d) Co_3O_4/FTO. (e) Calculation of number of moles of electrons transferred in the respective reduction peaks.

Table S4. OER overpotentials of all the materials explored in this work, on NF and FTO substrates, in this work, in 1 M KOH.

Material	Substrate	*j* (mA/cm^2)	*η* (mV)
Co_9S_8	NF	10	258 ± 3
		100	348 ± 2
	FTO	10	328 ± 4
$Co(OH)_2$	NF	10	298 ± 3
	FTO	10	361 ± 2
CoOOH	NF	10	340 ± 3
	FTO	10	405 ± 3
Co_3O_4	NF	10	352 ± 4
	FTO	10	507 ± 5

Table S5. Activity comparison of Co_9S_8 in this work with other reported cobalt sulfide based materials for OER in 1 M KOH.

Material	**Substrate**	**η_{10} (mV)**	**Reference**
Co_9S_8	***NF***	***258 ± 3***	***This work***
	FTO	***328 ± 2***	
Co_9S_8-$CoSe_2$	GC	340	[7]
N-CoS_2	N,S-G	260	[8]
CuCoS	CC	276	[9]
CoS_x	Co Foil	284	[10]
$CoNi_2S_4$	NF	328	[11]
CoS	Ti Foil	310	[12]
CoS	SS	300	[13]
Co-S	GC	312	[14]
$CuCo_2S_4$	GC	310	[15]
$Co_xNi_{1-x}S_2$	rGO	290	[16]
$Co_{0.5}Fe_{0.5}S$@N	GC	410	[17]
CoS_2	CP	290	[18]
Co_3S_4	CP	307	[18]
Co_9S_8	CP	342	[18]
CoS_2	CC	220	[19]
CoS	CC	310	[20]
Co_9S_8	GC	206	[21]
Co_3S_4	GC	360	[22]
Co-S films	NF	322	[23]
Co_3S_4@carbon	GC	250	[24]
Co_3S_4	S-doped rGO	341	[25]

N,S-G = N,S-co-doped graphene nanosheets, GC = Glassy Carbon, SS = Stainless Steel, rGO = reduced Graphene Oxide, CC = Carbon Cloth, CP = Carbon Paper

Table S6. The fitting parameter of the Nyquist plots (obtained from EIS) of the four materials on FTO, according to the given Randles equivalent circuit.

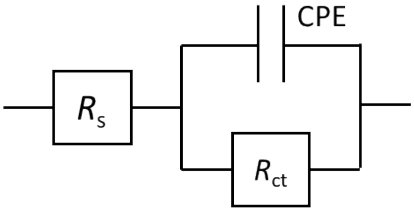

Material	***R*$_{ct}$ (Ω)**
Co_9S_8/FTO	6.2 ± 0.2
$Co(OH)_2$/FTO	10.3 ± 0.3
CoOOH/FTO	23.8 ± 0.1
Co_3O_4/FTO	12.1 ± 0.2

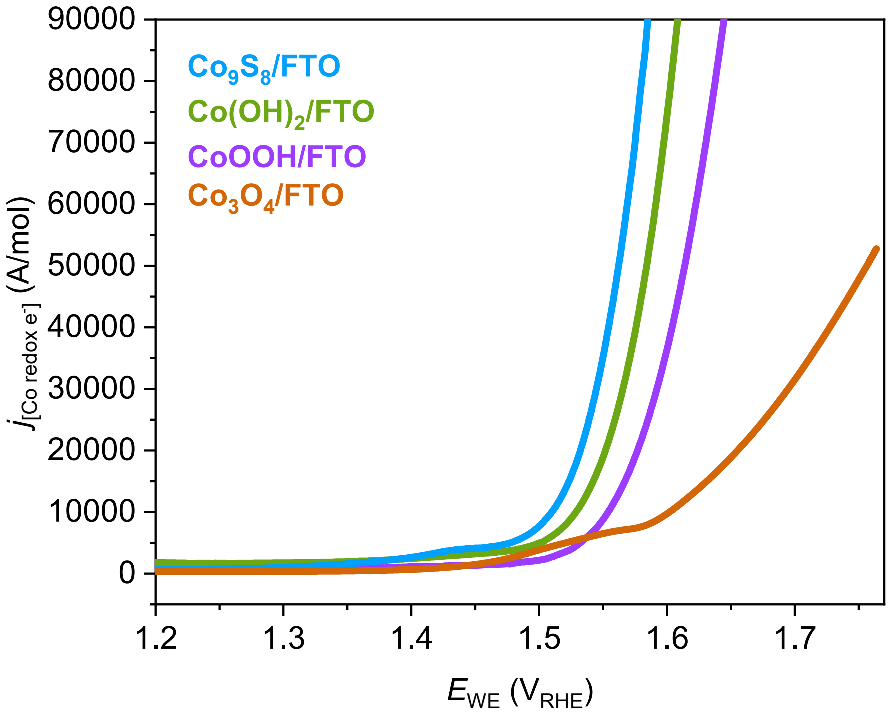

Figure S19. Normalization of the OER activity of Co_9S_8/FTO, $Co(OH)_2$/ FTO, CoOOH/ FTO, and Co_3O_4/ FTO by the number of moles of electrons transferred in the Co-redox features (Figure S18).

Table S7. Calculation of TOF of the materials on FTO.

Material	***j* at 1.63 V_{RHE} (mA/cm^2)**	**TOF (s^{-1})**
Co_9S_8/FTO	53.58	0.95
$Co(OH)_2$/FTO	28.38	0.73
CoOOH/FTO	8.79	0.35
Co_3O_4/FTO	3.40	0.076

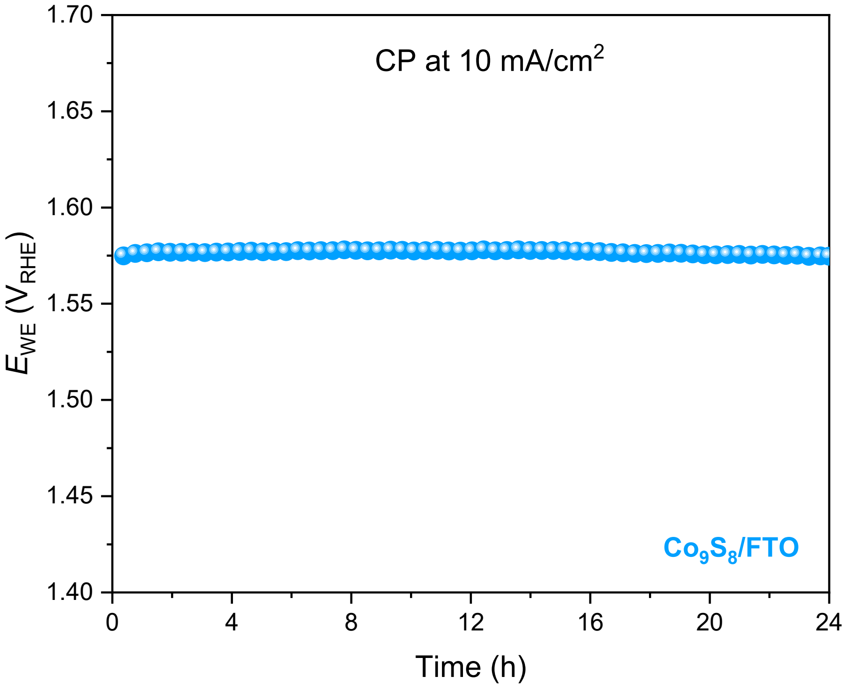

Figure S20. Co_9S_8/FTO showing a stable CP at 10 mA/cm^2 for 24 hours.

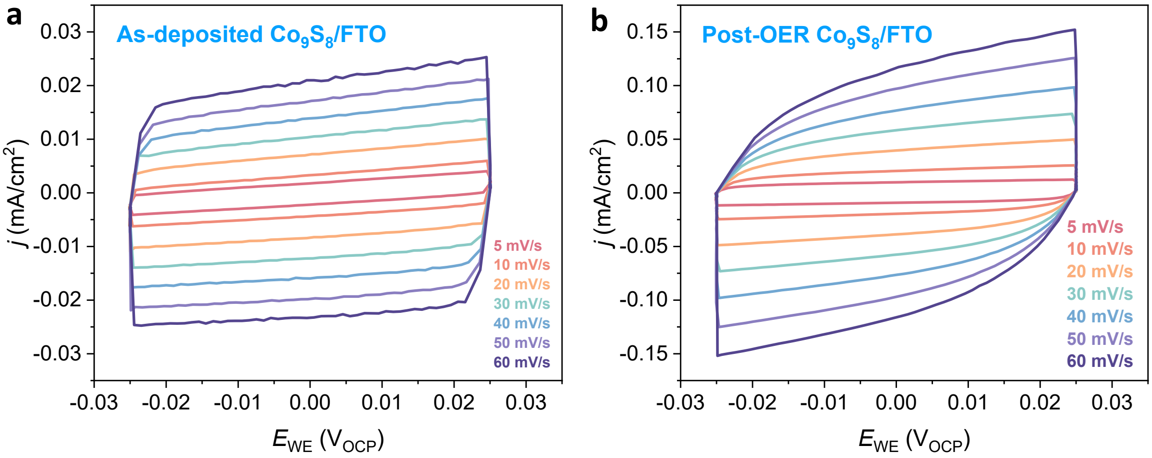

Figure S21. CVs recorded in the non-faradaic region for (a) as-deposited Co_9S_8/FTO, and (b) after 24 h CP at 10 mA/cm^2. All CVs were recorded at a scan rate of 5, 10, 20, 30, 40, 50 and 60 mV/s. The current densities and the difference between anodic and cathodic currents steadily increased with the scan rate. C_{dl} values were extracted from the plot of (anodic current-cathodic current)/2 at 0.00 V_{OCP} with respect to scan rate (shown in Figure 3e of the Manuscript).

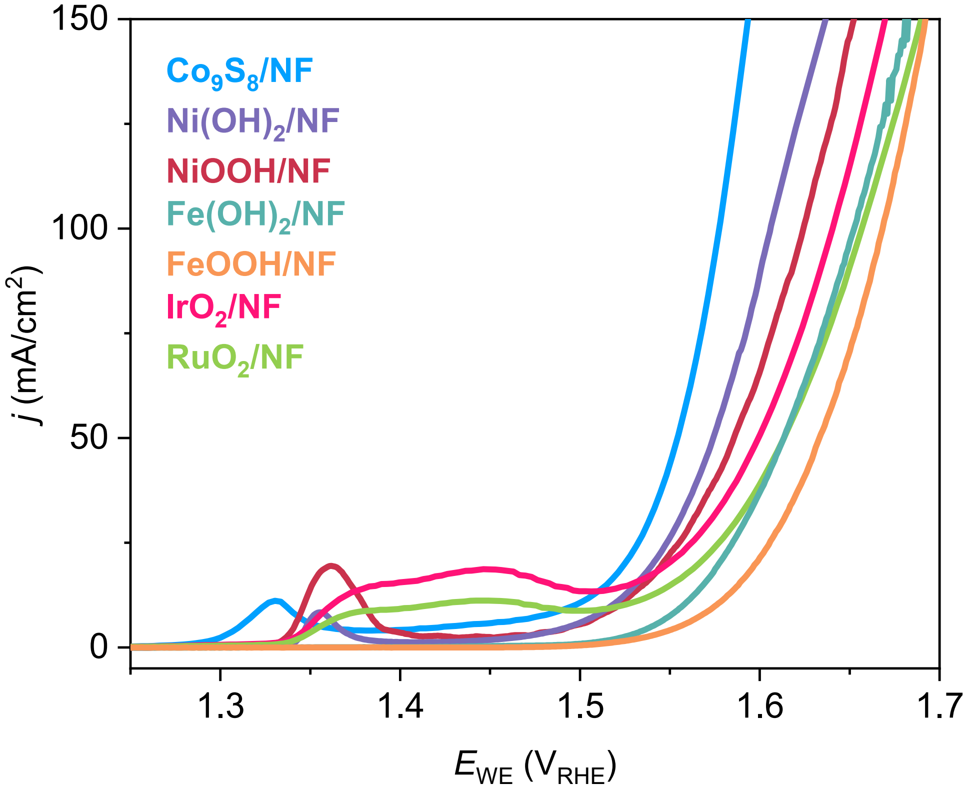

Figure S22. Comparison of OER LSV curves of Co_9S_8/NF with other Ni, Fe, and noble metal-based catalysts deposited on NF, at a scan rate of 3 mV/s, in identical conditions.

Table S8. Faradaic efficiency for OER of Co_9S_8 /NF.

Material	j (mA/cm^2)	t (s)	V_{O2} (mL)	FE (O_2,%)
Co_9S_8/NF	49.3	3600	10.82	96 ± 3

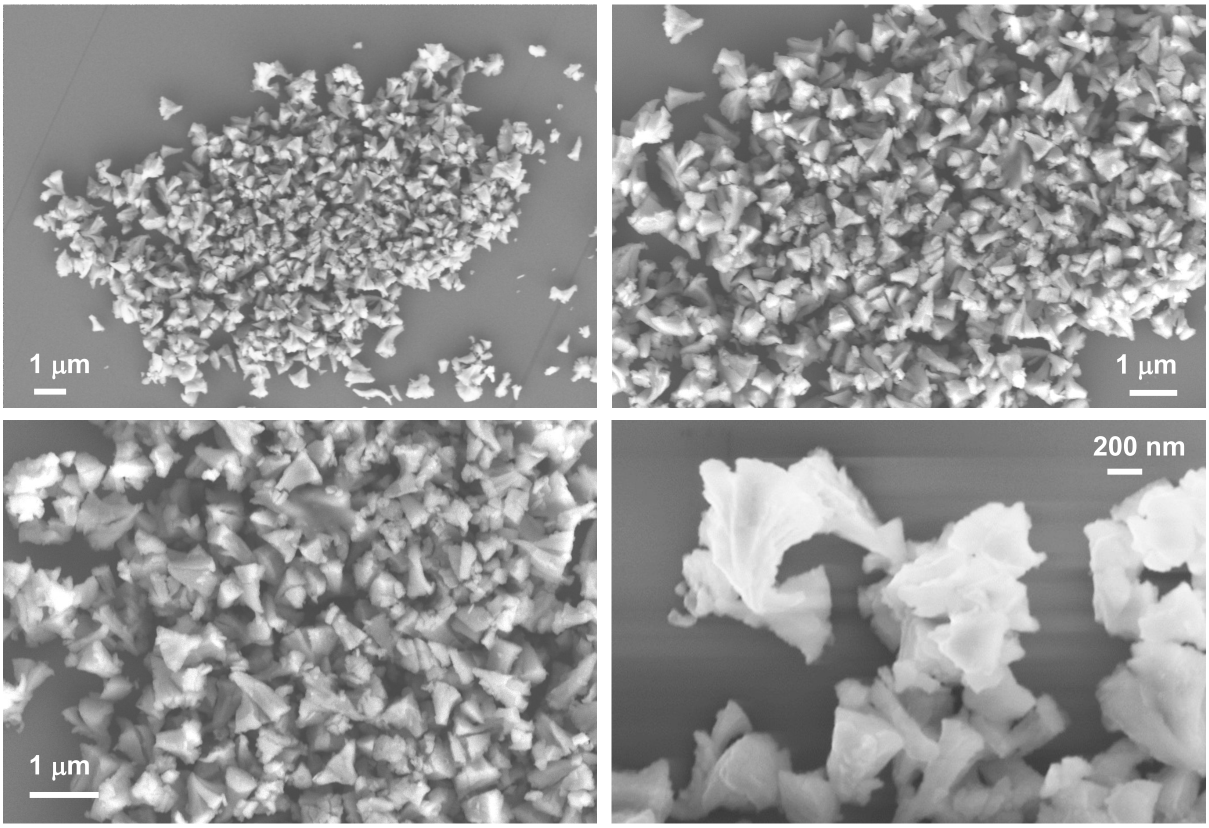

Figure S23. SEM images of Co_9S_8 after 24 h CP at 10 mA/cm^2 (recorded by scratching off the film from FTO) at different magnifications. A complete transformation of the material to distorted triangle-like agglomerates occurs during OER.

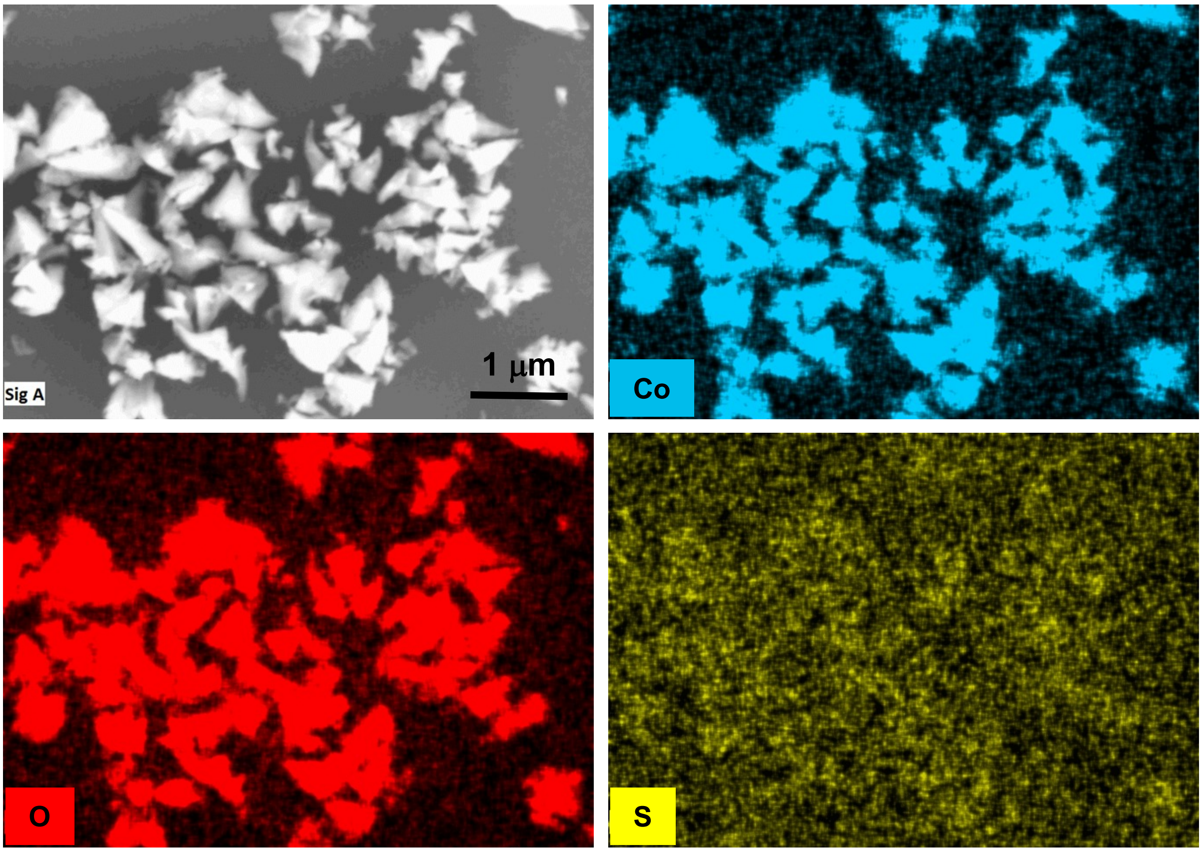

Figure S24. SEM image and elemental mapping of Co_9S_8 after 24 h CP at 10 mA/cm^2 (recorded by scratching off the film from FTO) shows a homogeneous distribution of Co (blue), and O (red) in the sample. S mapping (yellow) exhibits the presence of only a trace amount of S in the catalyst.

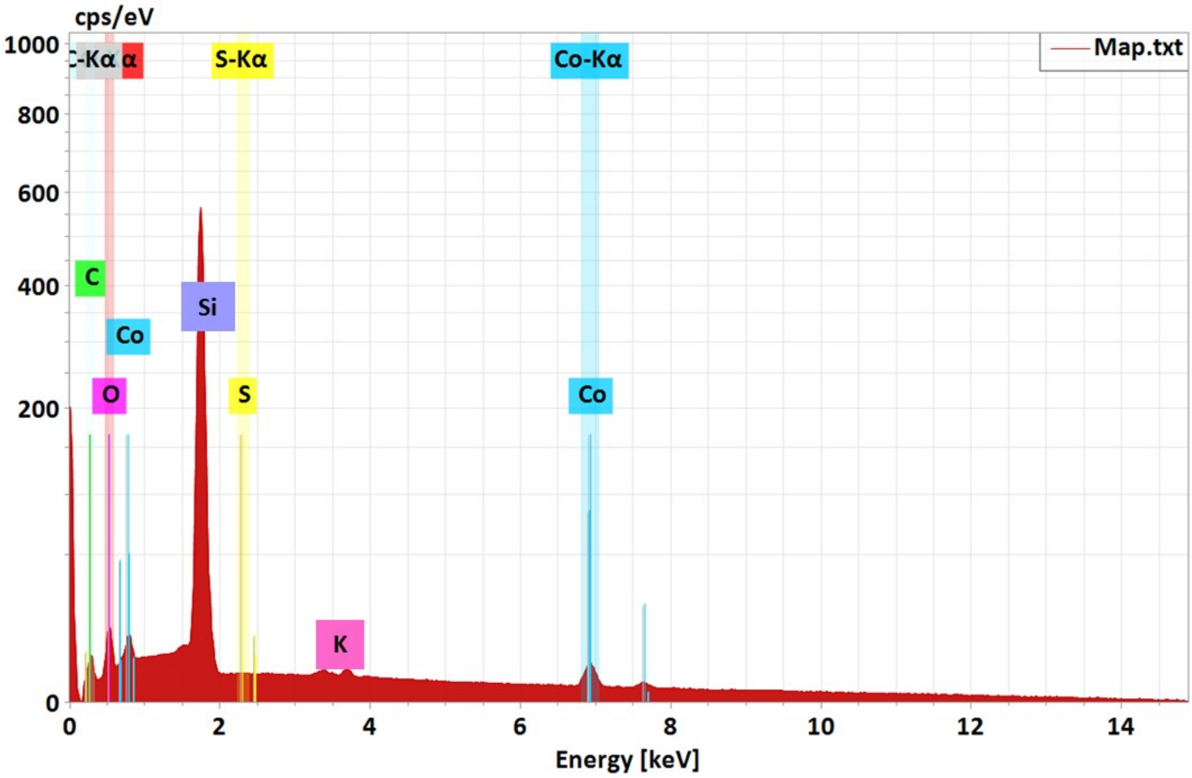

Figure S25. EDX spectrum of Co_9S_8 after 24 h OER CP at 10 mA/cm^2 (recorded by scratching off the film from FTO), wherein only a trace amount of S (Co:S ratio of 1:0.01) is present. The Si peak comes from the Si wafer substrate. Residual K from the KOH electrolyte appears as adsorbed species on the surface of the catalyst.

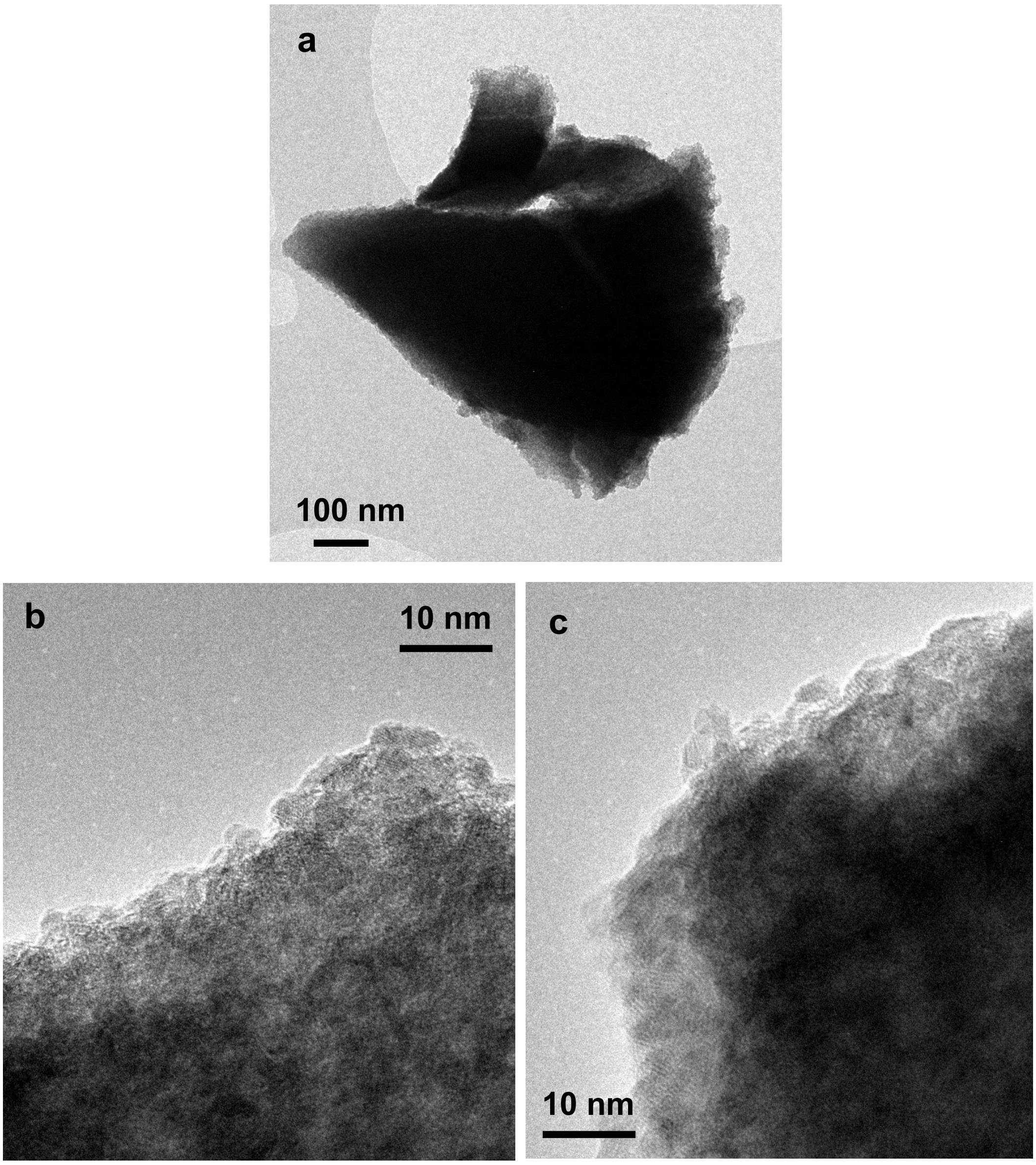

Figure S26. (a) TEM and (c, d) HR-TEM images of Co_9S_8 after 24 h OER CP at 10 mA/cm^2 show a complete transformation of the material from a hexagon-like shape to a distorted triangle-like shape after OER. The HR-TEM images also show lattice fringes of the cobalt (oxy)hydroxide phase, as supported by the SAED (Figure 4c of the Manuscript).

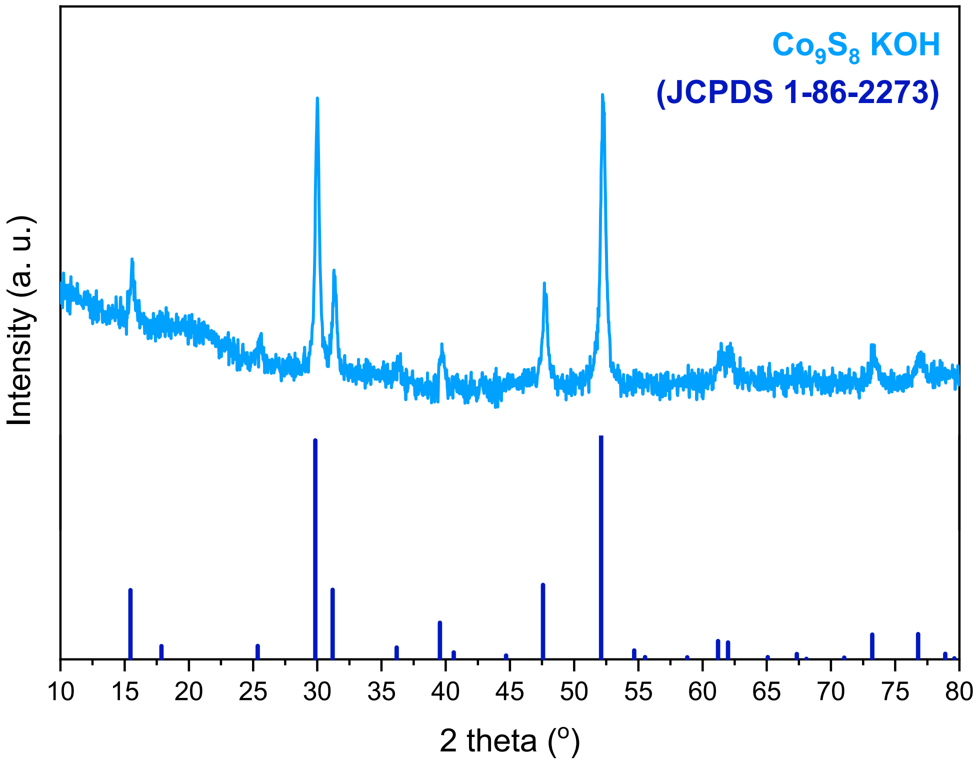

Figure S27. pXRD pattern of Co_9S_8 after exposing to 1 M KOH electrolyte for 2 hours, shows no discernible change in the crystalline structure of the material compared to as-prepared Co_9S_8.

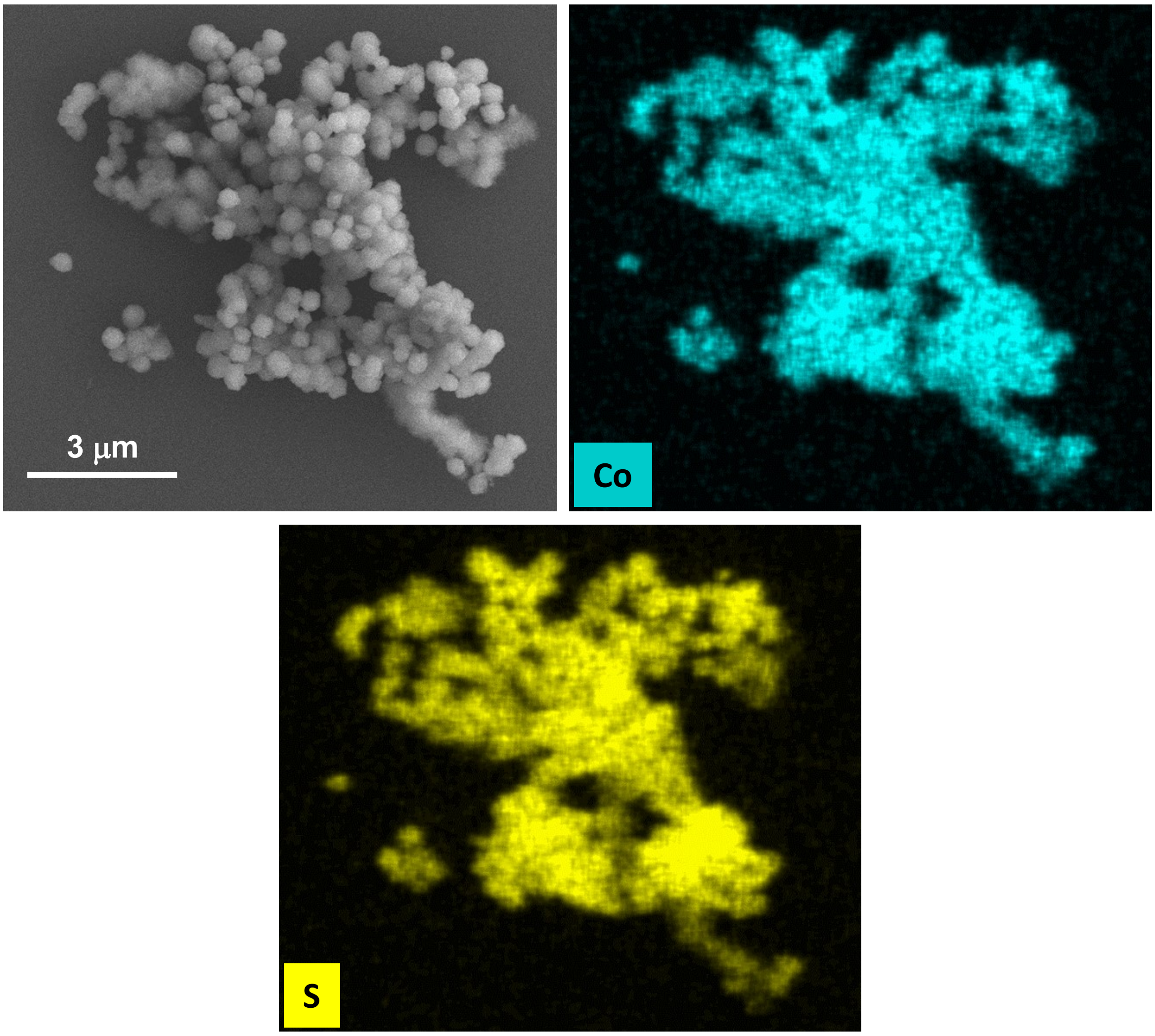

Figure S28. SEM image and elemental mapping of Co_9S_8 after exposing to 1 M KOH electrolyte for 2 hours shows a retention of the morphology and the homogeneous distribution of Co (blue), and S (yellow) in the sample, similar to the as-prepared Co_9S_8.

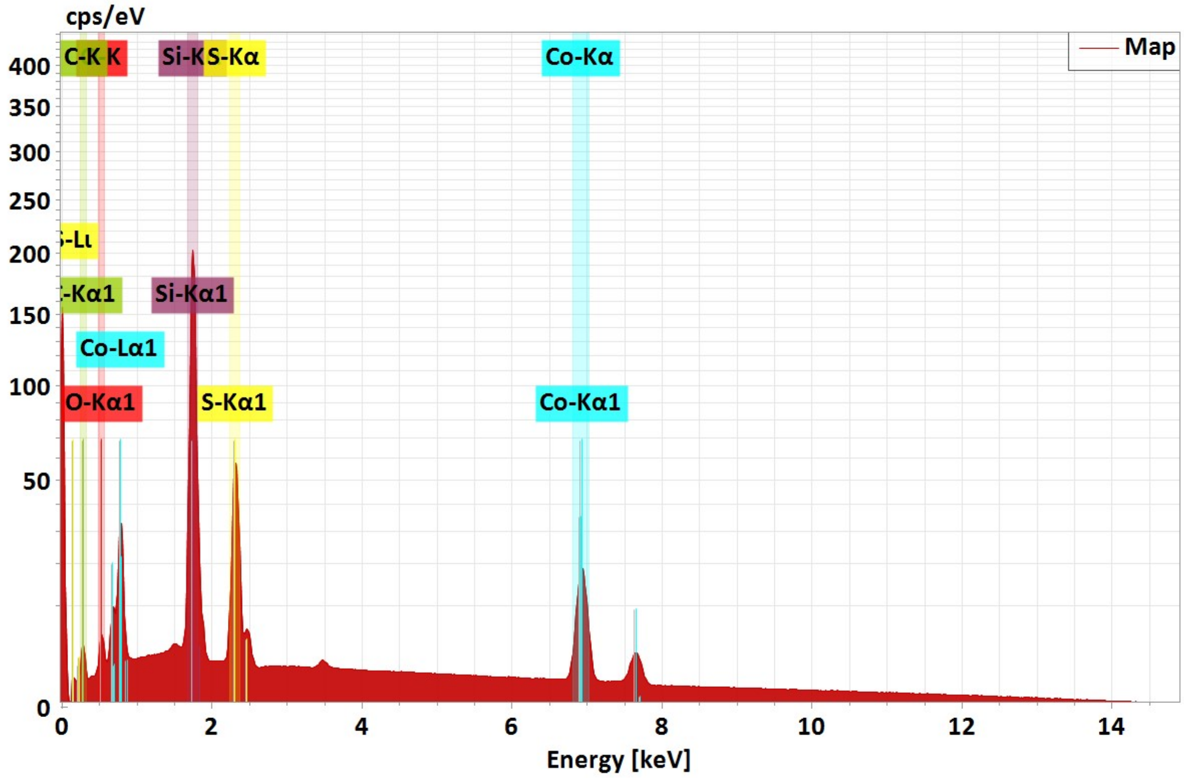

Figure S29. EDX spectrum of Co_9S_8 after exposing to 1 M KOH electrolyte for 2 hours shows a retention of the Co:S ratio of 1:0.89 in the sample, similar to the as-prepared Co_9S_8.

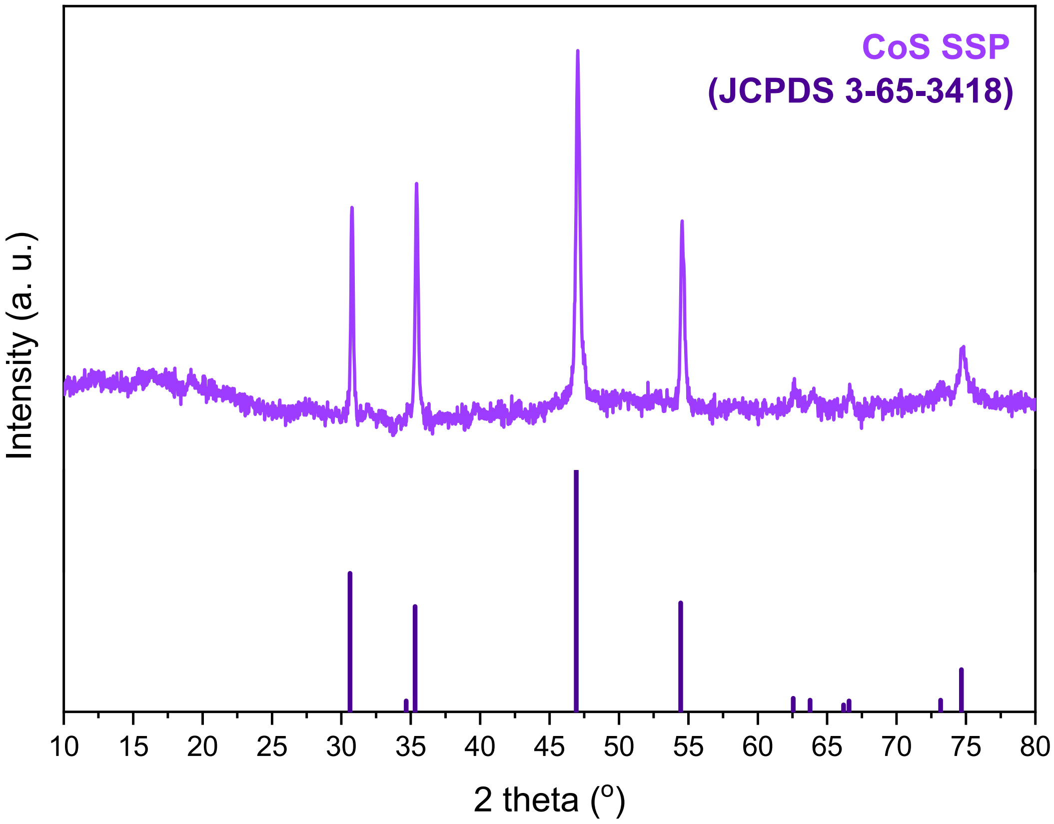

Figure S30. pXRD pattern of CoS phase derived from SSP complex **1**.

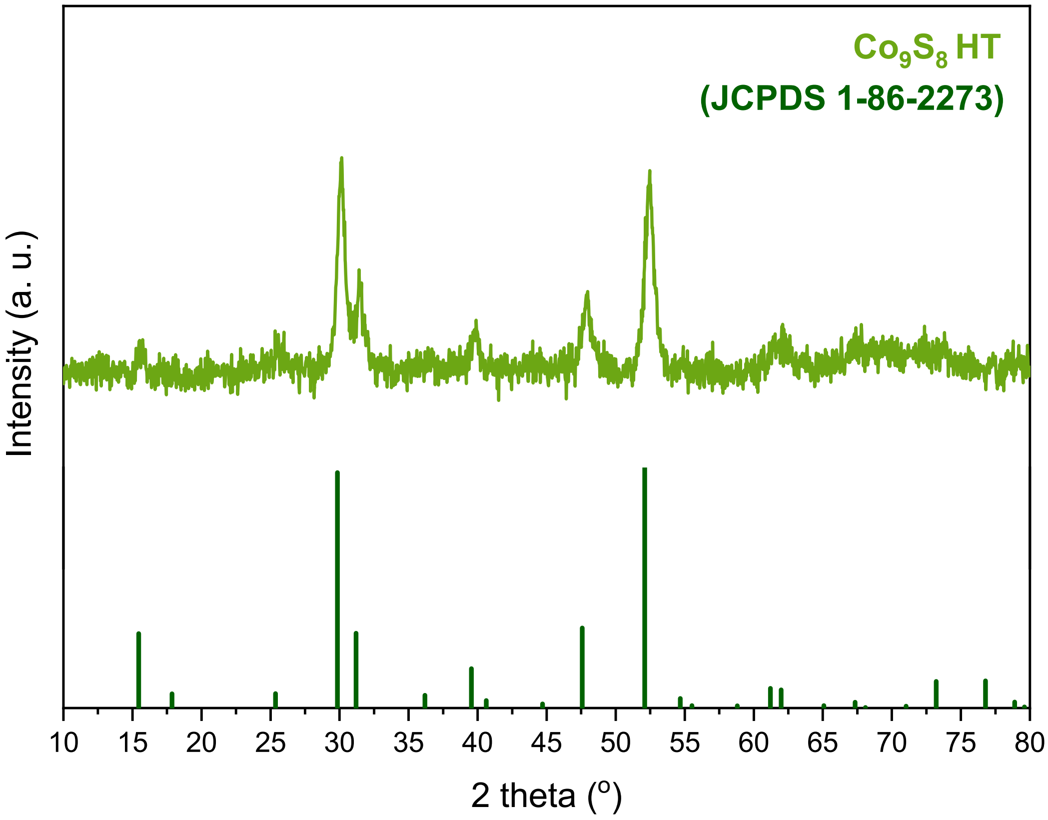

Figure S31. pXRD pattern of hydrothermally (HT) synthesized Co_9S_8 phase.

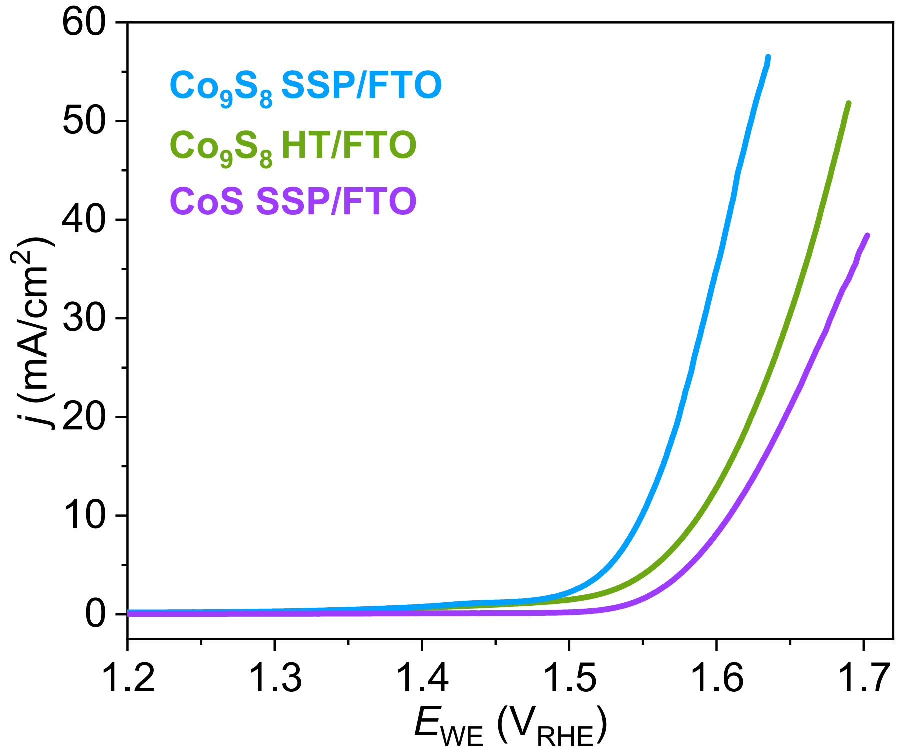

Figure S32. Comparison of OER LSV curves of single-source precursor (SSP)-derived Co_9S_8 with hydrothermally-derived Co_9S_8 and SSP-derived CoS deposited on FTO, in 1 M KOH, at a scan rate of 5 mV/s.

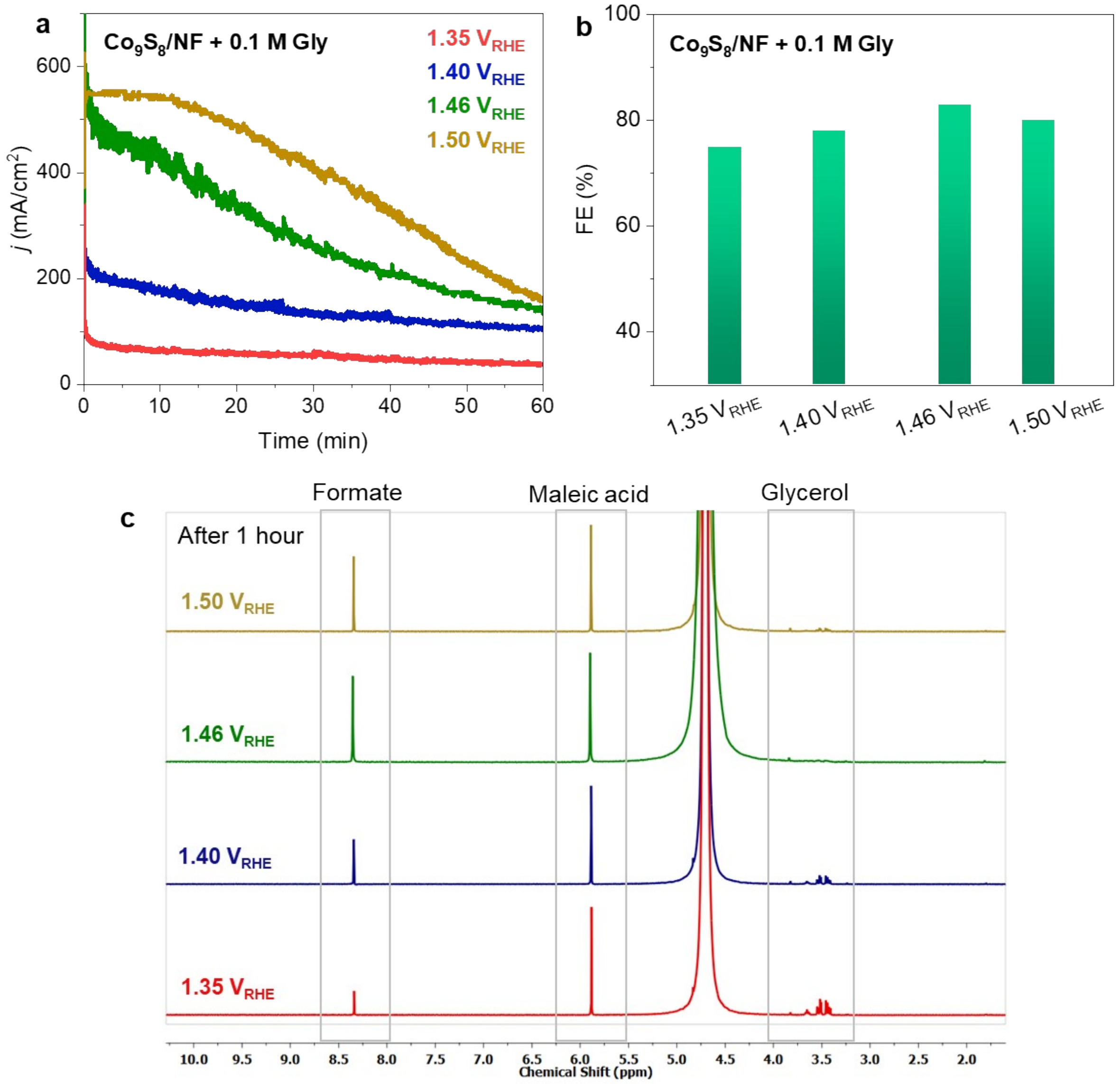

Figure S33. (a) CA curves for the bulk electrolysis of 0.1 M glycerol in 15 ml of 1 M KOH with Co_9S_8/NF at different potentials for 60 minutes, and their corresponding (b) FEs and (c) NMR data.

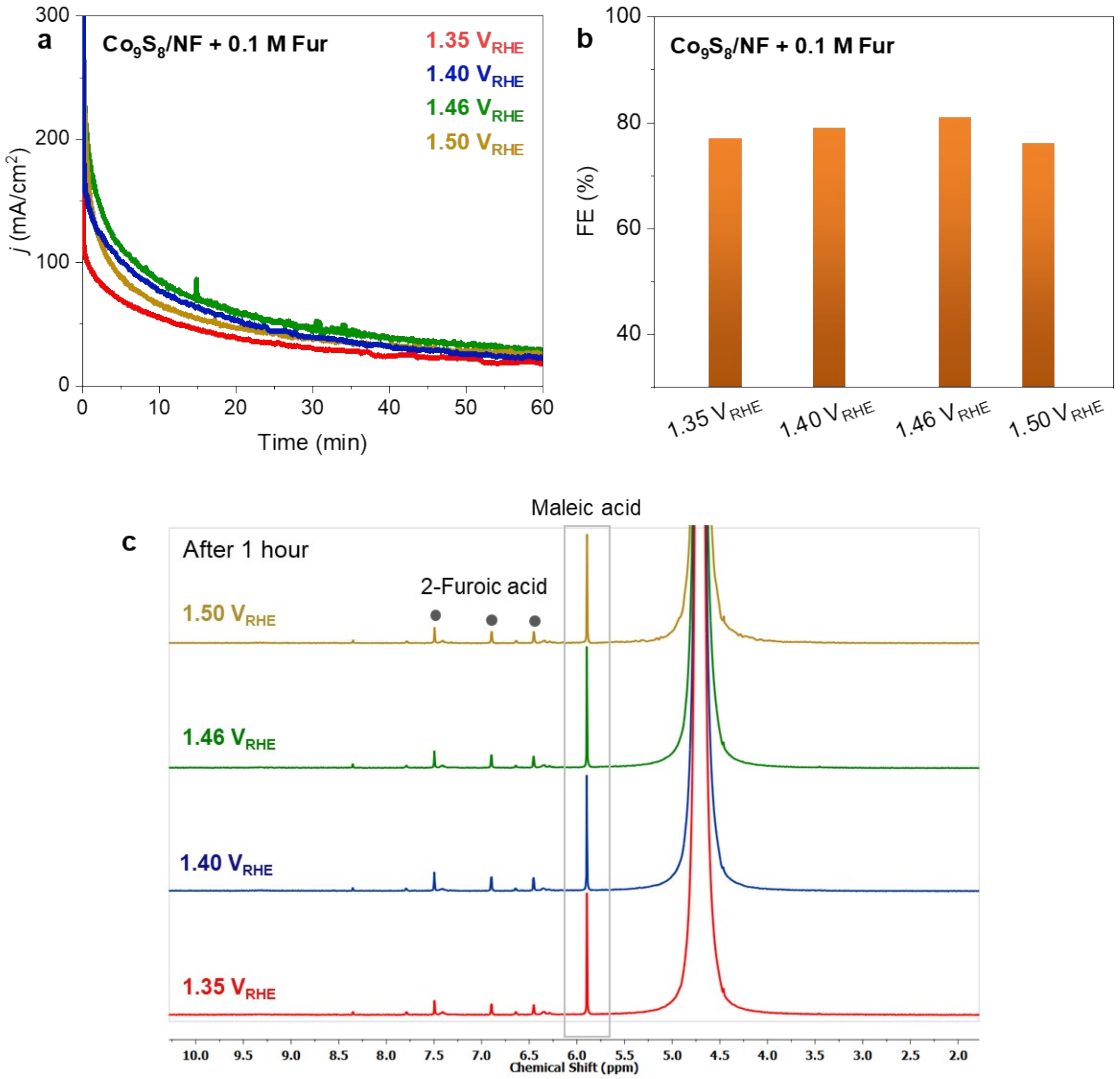

Figure S34. (a) CA curves for the bulk electrolysis of 0.1 M furfural in 15 ml of 1 M KOH with Co_9S_8/NF at different potentials for 60 minutes, and their corresponding (b) FEs and (c) ^{1}H NMR data.

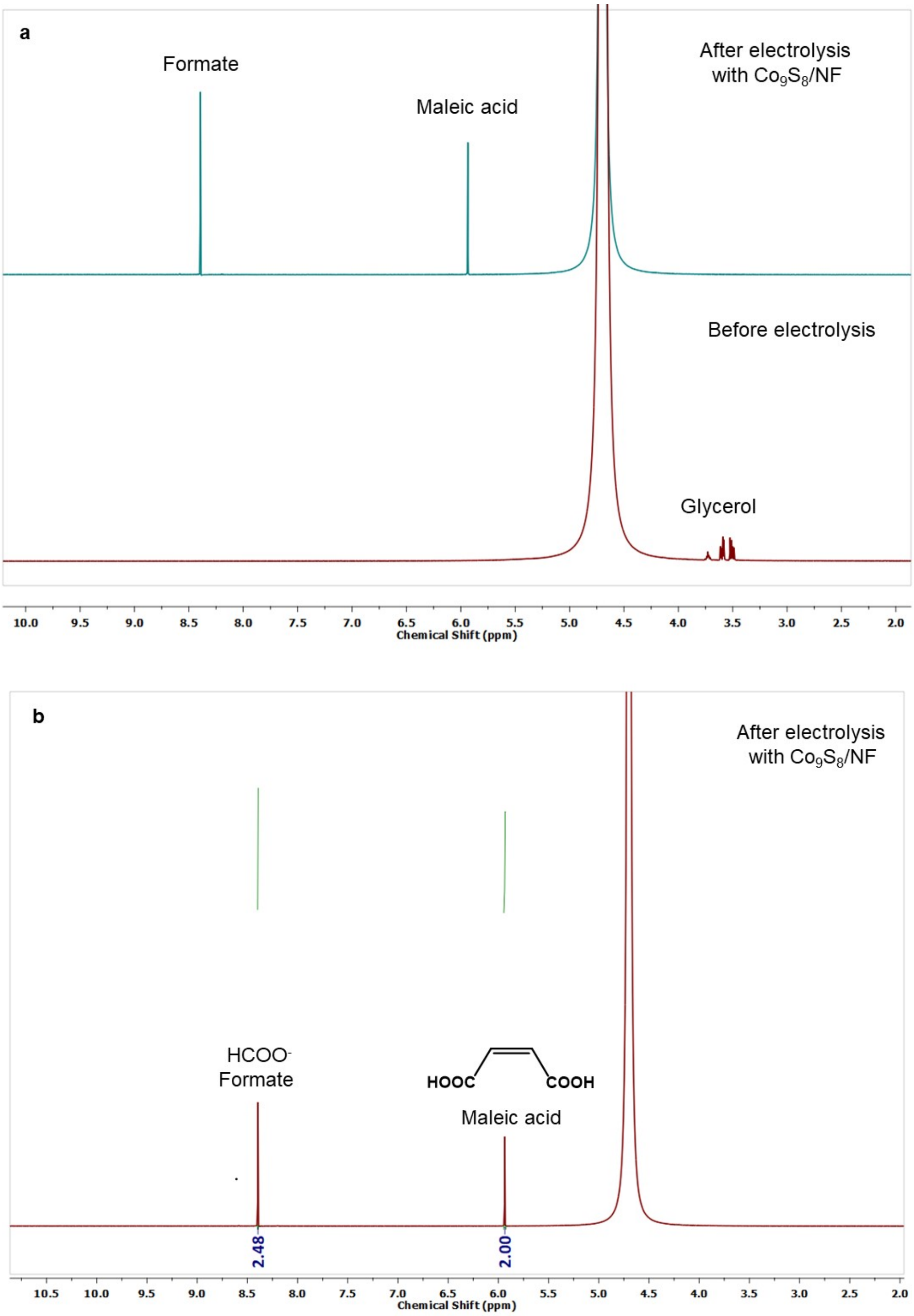

Figure S35. (a) The ^{1}H NMR spectra of 0.1 M glycerol electrolyte before and after bulk electrolysis (at 1.46 V_{RHE} for 140 min) with Co_9S_8/NF; (b) Detailed ^{1}H NMR spectrum of 0.1 M glycerol electrolyte after bulk electrolysis with Co_9S_8/NF, wherein the peak at 8.39 ppm can be assigned to formate (product). The integral values of the internal standard (maleic acid) revealed an 83% conversion of glycerol to formate.

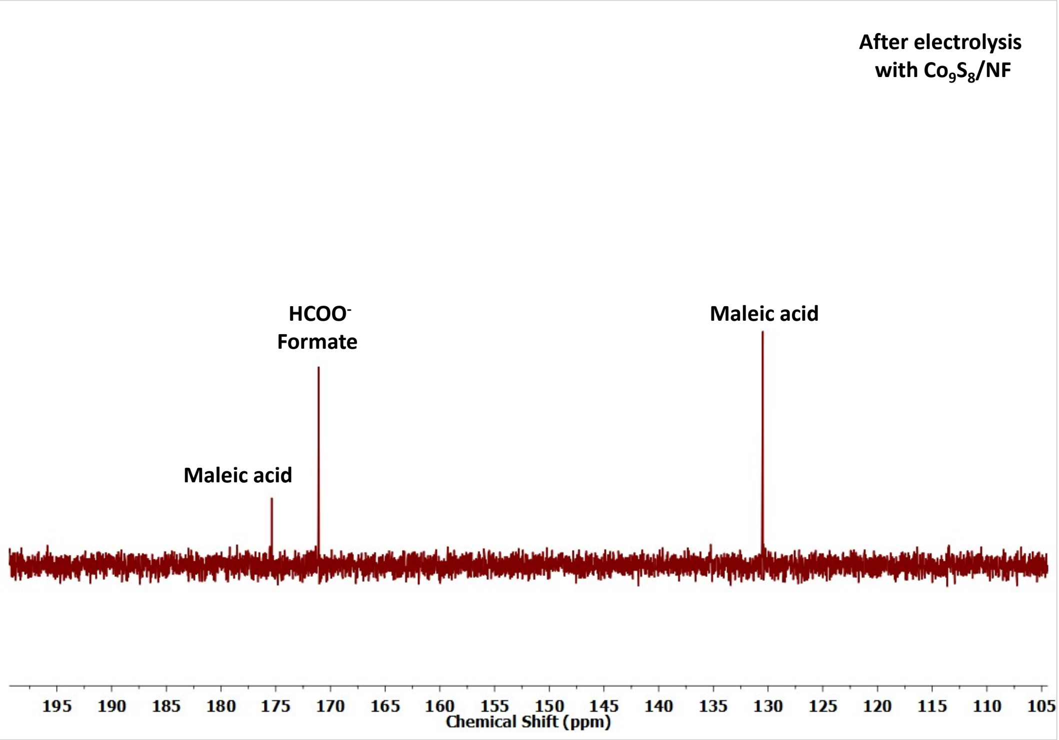

Figure S36. ^{13}C NMR spectra of 0.1 M glycerol electrolyte after bulk electrolysis (at 1.46 V_{RHE} for 140 min) with Co_9S_8/NF, and maleic acid as the internal standard. The spectrum shows the formation of only formate and the absence of carbonates and any other C-based side products.

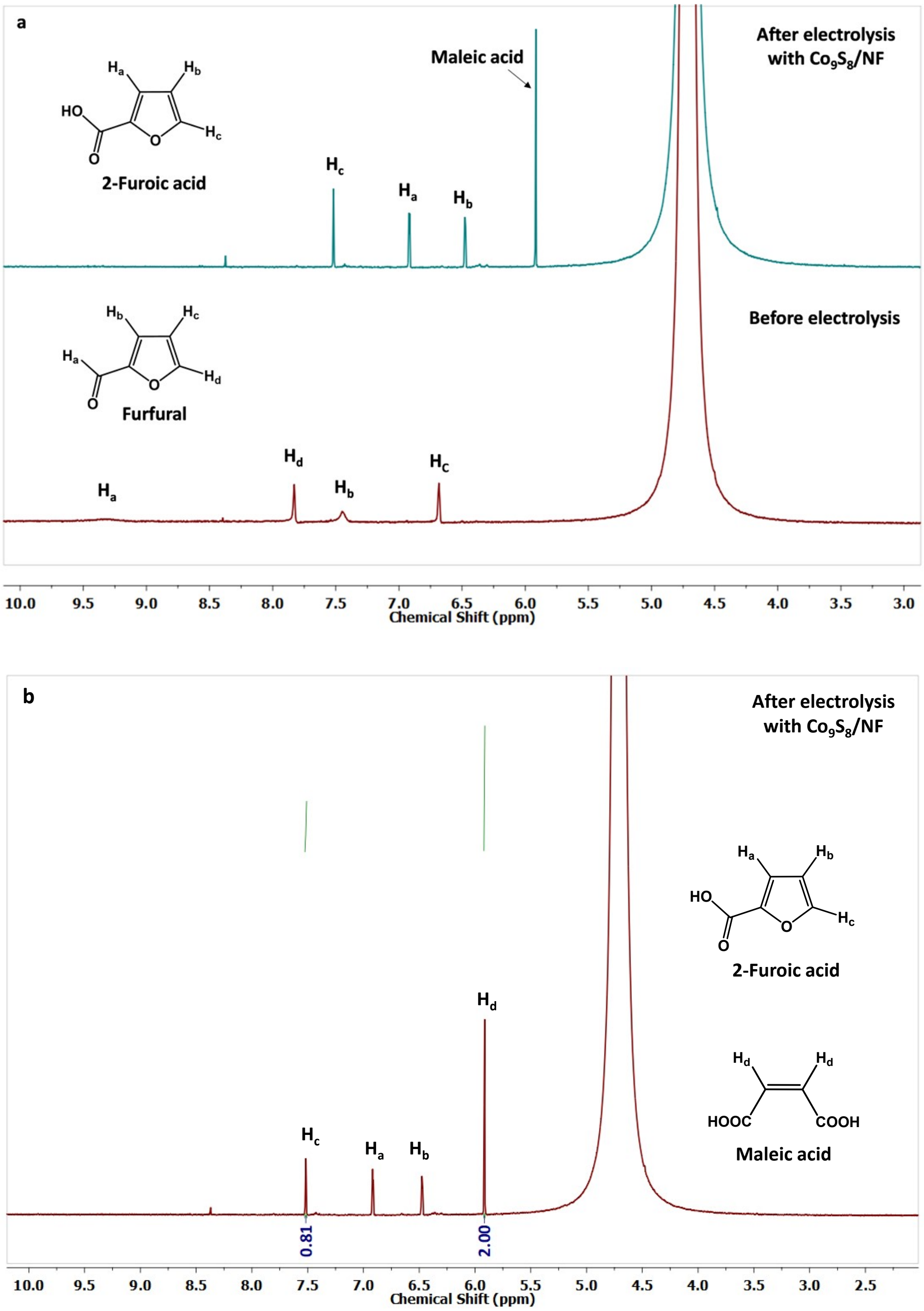

Figure S37. (a) The ^{1}H NMR spectra of 0.1 M furfural electrolyte before and after bulk electrolysis (at 1.46 V_{RHE} for 145 min) with Co_9S_8/NF; (b) Detailed ^{1}H NMR spectrum of 0.1 M furfural electrolyte after bulk electrolysis with Co_9S_8/NF, wherein the peaks between 6.4-7.6 ppm can be assigned to furoic acid (product). The integral values of the internal standard (maleic acid) revealed an 81% conversion of furfural to 2-furoic acid.

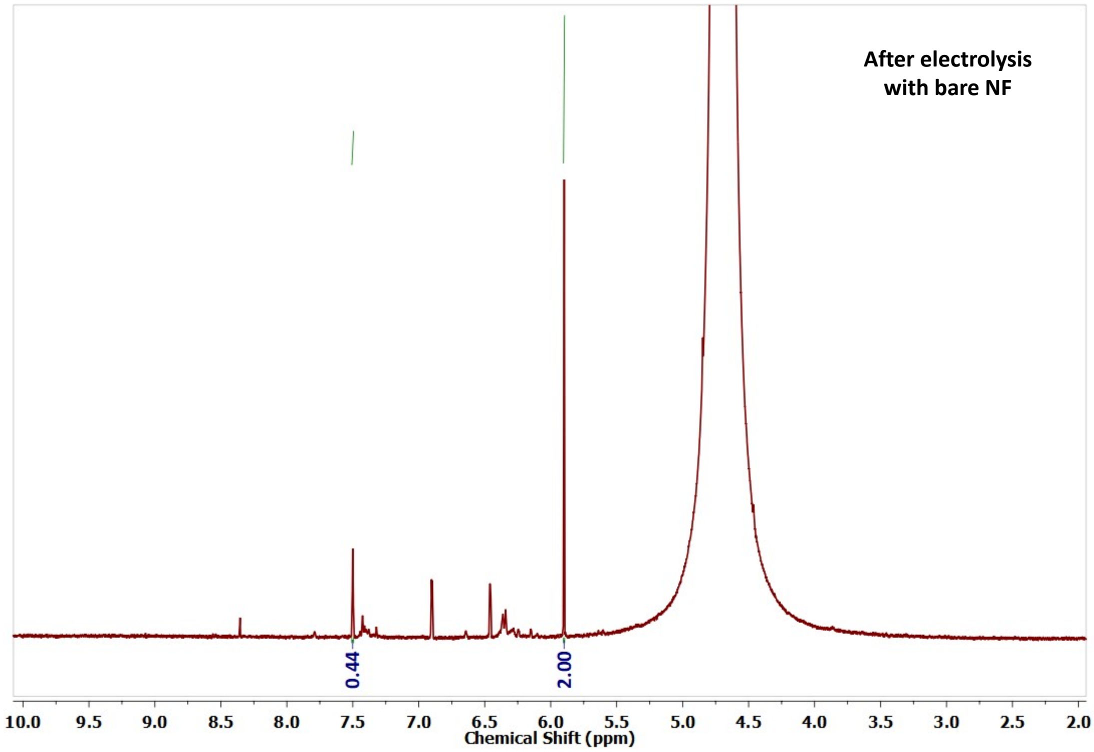

Figure S38. The ^{1}H NMR spectra of 0.1 M furfural electrolyte after bulk electrolysis (at 1.46 V_{RHE} for 145 min) with bare NF. The integral values of the internal standard (maleic acid) revealed a 44% conversion of furfural to 2-furoic acid.

Table S9. Comparison of glycerol to formate oxidation performance of Co_9S_8 in this work with reported cobalt and other transition metal-based materials.

Material	**Substrate**	**Conc. of glycerol (M)**	**Potential (V_{RHE})**	**Yield rate of formate ($mmol^{-1}$ h^{-1} cm^{-2})**	**FE (%)**	**Ref**
Co_9S_8	***NF***	***0.1***	***1.46***	***0.355 $mmol_{formate}$ $mmol_{glycerol}^{-1}$ h^{-1} cm^{-2}***	***83***	***This work***
$CoSe_2$	CC	1.0	1.48	1.4162	90	26
$NiCo_2O_4$	NF	0.1	1.80	3.385	>97	27
$NiFe_2O_4$	NF	0.1	1.80	2.284	>94	27
$Co(OH)_2$-SDS	NF	0.1	1.42	0.35	80	28
$NiCo_2O_4$	NF	0.1	1.40	5.69	89.9	29
Co_3O_4	NF	0.1	1.40	1.29	61	29
NiO	NF	0.1	1.40	0.60	86.7	29
Ni_2CoO_4	NF	0.1	1.40	1.77	76.9	29
$Ni(OH)_2$	NF	0.1	1.36	0.55	96.9	30
amorphous NiFe-LDH	NF	0.1	1.47	0.434	99.03	31
crystallized NiFe-LDH	NF	0.1	1.47	0.05	<80	31
LiFeBPO	NF	0.1	1.46	0.565	99	32
$Ni_{0.33}Co_{0.67}(OH)_2$@HOS	NF	0.1	1.35	-	96	33
Pt_{SA}-NiCo LDH	NF	0.1	1.375	-	88.7	34
Cu-CuS	BM	0.1	1.45	-	90.4	35
Mn-CoN@C	NF	0.3	1.35	-	97.7	36
$ZnFe_xCo_{2-x}O_4$ ($x = 0$ to 1.5)	CP	0.5	1.524	-	~50-55	37

HEA = High Entropy Alloy, SDS = Sodium Dodecyl Sulfate, LDH = Layer double hydroxide, BM = Brass Mesh

Table S10. Comparison of furfural to 2-furoic acid oxidation performance of Co_9S_8 in this work with reported cobalt and transition metal-based materials.

Material	**Substrate**	**Conc. of glycerol (M)**	**Potential (V_{RHE})**	**Yield rate of 2-furoic acid**	**FE (%)**	**Ref**
Co_9S_8	***NF***	***0.1***	***1.46***	***0.335 $mmol_{2\text{-}furoic\ acid}$ $mmol_{furfural}^{-1}$ h^{-1} cm^{-2}***	***83***	***This work***
P-NF-10	NF	0.1	1.49	0.867 mmol h^{-1} cm^{-2}	94	[38]
Pt-Co_3O_4	CC	0.05	1.55	6.6 mM h^{-1}	66.1	[39]
Co_3O_4	CC	0.05	1.55	3.2 mM h^{-1}	34.8	[39]
Ir–CuO	CC	0.05	1.58	10.85 mM h^{-1}	72.7	[40]
Pd–CuO	CC	0.05	1.58	6.59 mM h^{-1}	39.1	[40]
Ru–CuO	CC	0.05	1.58	8.31 mM h^{-1}	43.8	[40]
CuO	CC	0.05	1.58	8.21 mM h^{-1}	60.4	[40]
Ni_2P/Ni	NF	0.03	1.423	-	100	[41]
Mixed-valence Cu		0.05	0.3	-	100	
Cu_3P	CFC	0.05	1.50	-	>85	[42]
Ni_2P	CFC	0.05	1.50	-	>85	[42]
Pt/C	CC	0.1	0.90	-	40	[43]

CFC = Carbon Fibre Cloth

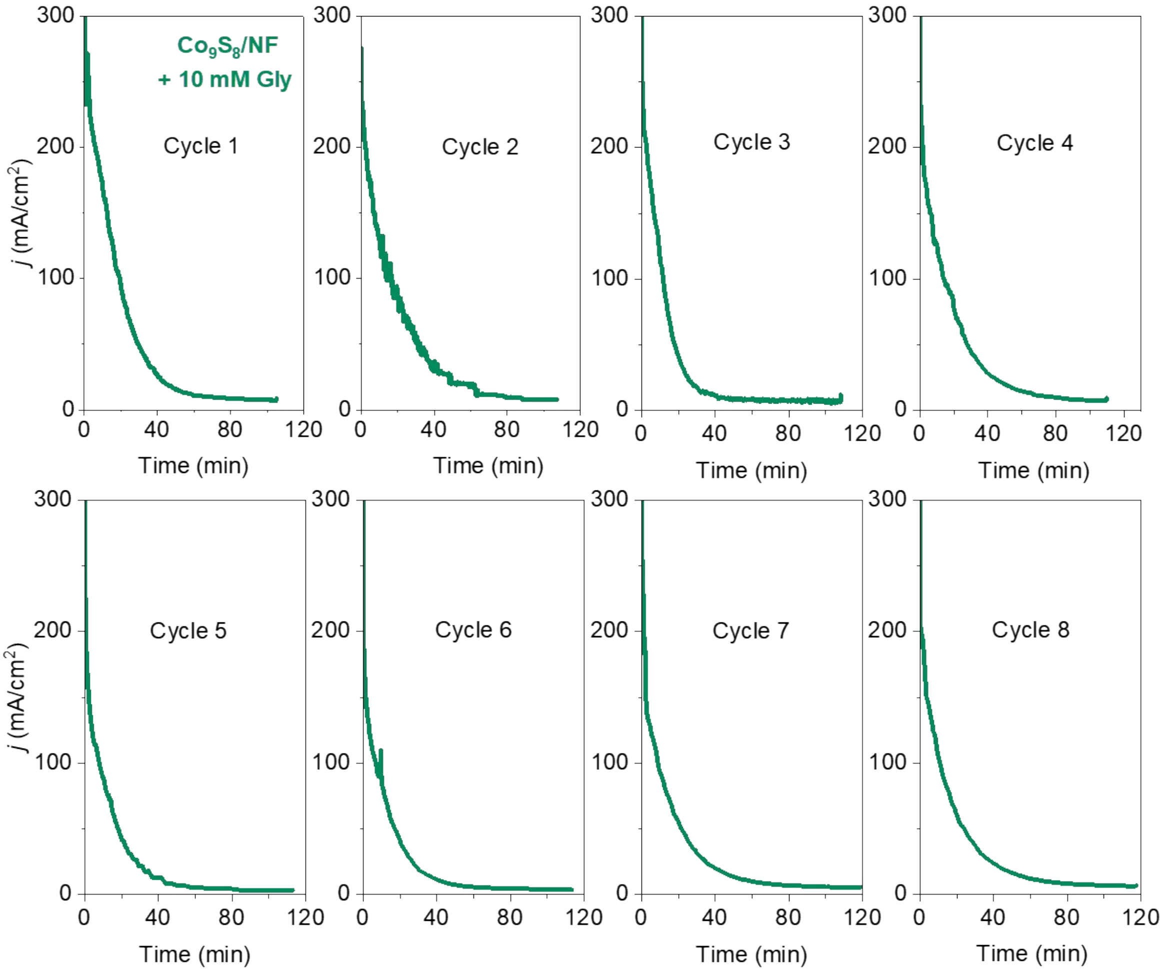

Figure S39. CA bulk electrolysis measurements for Co_9S_8/NF with 10 mM glycerol in 15 mL of 1 M KOH for 8 consecutive cycles, until the charge required for the full conversion is passed (115.8 C).

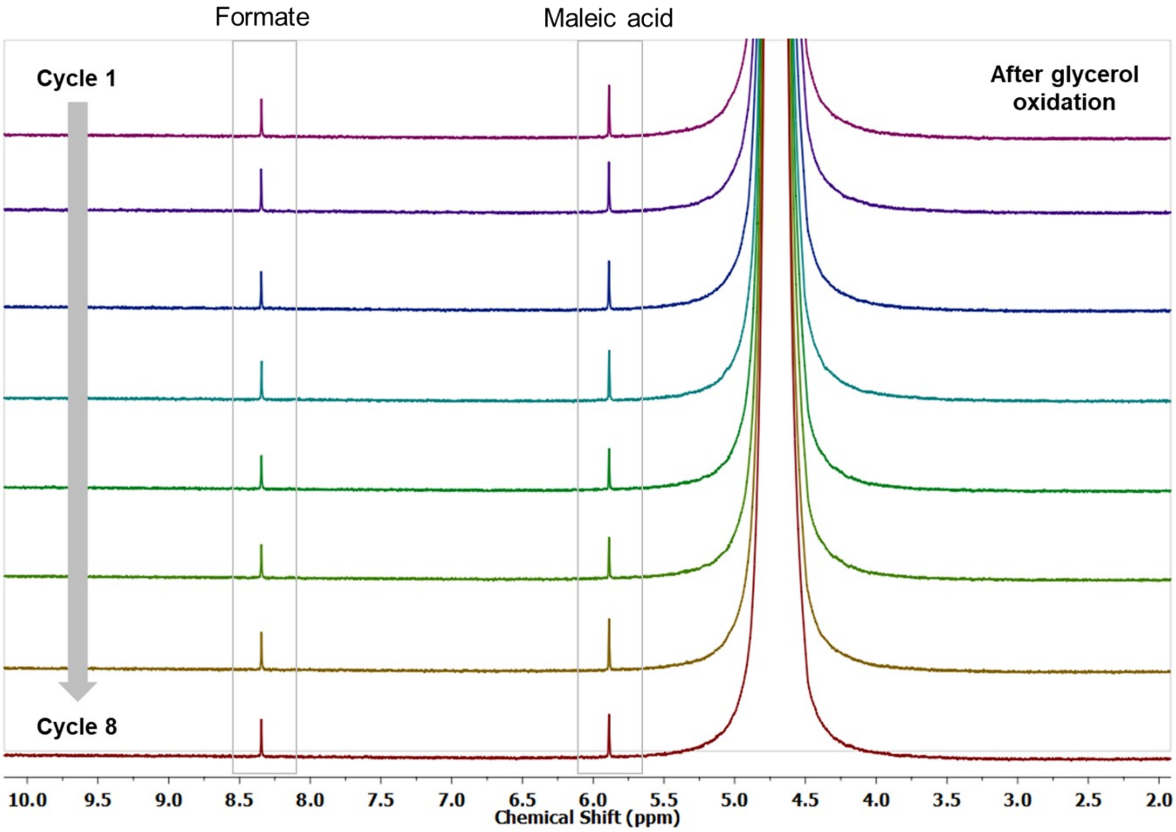

Figure S40. ^{1}H NMR data for Co_9S_8/NF after bulk electrolysis with 10 mM glycerol in 15 mL of 1 M KOH for 8 consecutive cycles.

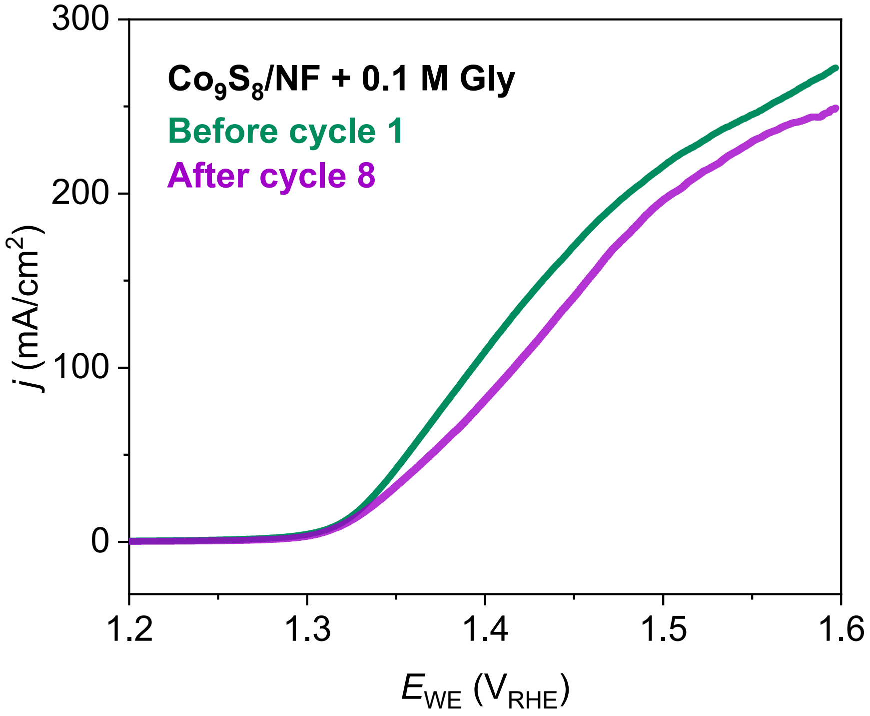

Figure S41. LSV curves for Co_9S_8/NF with 10 mM glycerol in 15 mL of 1 M KOH, at a scan rate of 5 mV/s, before the 1st CA measurement and after the 8th CA measurement.

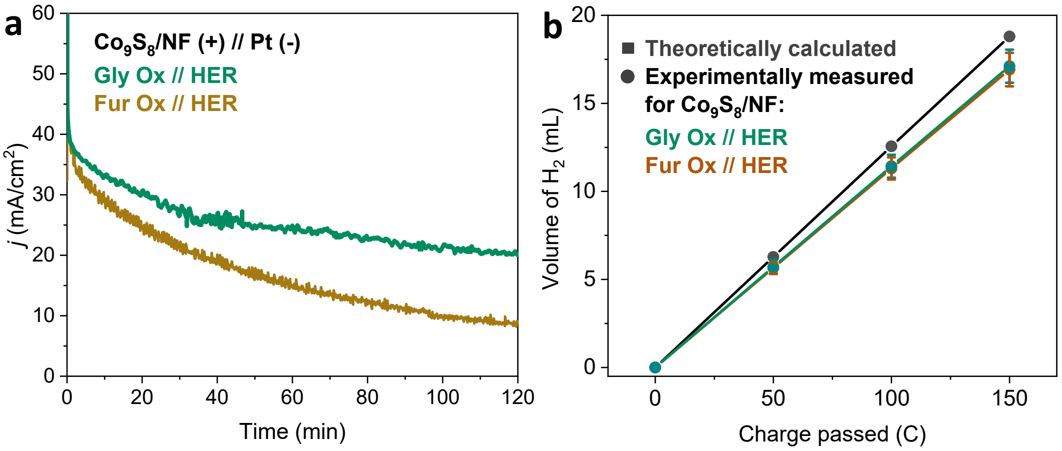

Figure S42. (a) CA curves for the bulk electrolysis of 0.1 mM glycerol/ furfural in 15 mL of 1 M KOH with Co_9S_8/NF anode coupled with HER in pure 1 M KOH with Pt wire. (b) The theoretically calculated and experimentally obtained volume of H_2 with passing charge for the Gly Ox // HER and Fur Ox // HER full cells.

References

1 G. M. Sheldrick, *Acta Crystallogr. Sect. A Found. Adv.*, 2015, **71**, 3–8.

2 O. V. Dolomanov, L. J. Bourhis, R. J. Gildea, J. A. K. Howard and H. Puschmann, *J. Appl. Crystallogr.*, 2009, **42**, 339–341.

3 J. N. Hausmann, B. Traynor, R. J. Myers, M. Driess and P. W. Menezes, *ACS Energy Lett.*, 2021, **6**, 3567–3571.

4 S. Niu, S. Li, Y. Du, X. Han and P. Xu, *ACS Energy Lett.*, 2020, **5**, 1083–1087.

5 S. Anantharaj, S. Noda, M. Driess and P. W. Menezes, *ACS Energy Lett.*, 2021, **6**, 1607–1611.

6 B. Dasgupta, J. N. Hausmann, R. Beltrán-Suito, S. Kalra, K. Laun, I. Zebger, M. Driess and P. W. Menezes, *Small*, 2023, **19**, 2301258.

7 S. Chakrabartty, S. Karmakar and C. R. Raj, *ACS Appl. Nano Mater.*, 2020, **3**, 11326–11334.

8 Y. Tong, Q. Sun, P. Chen, L. Chen, Z. Fei and P. J. Dyson, *ChemSusChem*, 2020, **13**, 5112–5118.

9 H. Luo, H. Lei, Y. Yuan, Y. Liang, Y. Qiu, Z. Zhu and Z. Wang, *Catalysts*, 2019, **9**, 459.

10 H. Bian, T. Chen, Z. Chen, J. Liu, Z. Li, P. Du, B. Zhou, X. Zeng, J. Tang and C. Liu, *Electrochim. Acta*, 2021, **389**, 138786.

11 J. Li, Q. Zhuang, P. Xu, D. Zhang, L. Wei and D. Yuan, *Chinese J. Catal.*, 2018, **39**, 1403–1410.

12 K. Nan, H. Du, L. Su and C. M. Li, *ChemistrySelect*, 2018, **3**, 7081–7088.

13 S. B. Kale, A. C. Lokhande, R. B. Pujari and C. D. Lokhande, *J. Colloid Interface Sci.*, 2018, **532**, 491–499.

14 S. Ju, Y. Liu, H. Chen, F. Tan, A. Yuan, X. Li and G. Zhu, *ACS Appl. Energy Mater.*, 2019, **2**, 4439–4449.

15 M. Chauhan, K. P. Reddy, C. S. Gopinath and S. Deka, *ACS Catal.*, 2017, **7**, 5871–5879.

16 Y. R. Hong, S. Mhin, K. M. Kim, W. S. Han, H. Choi, G. Ali, K. Y. Chung, H. J. Lee, S. I. Moon, S. Dutta, S. Sun, Y. G. Jung, T. Song and H. S. Han, *J. Mater. Chem. A*, 2019, **7**, 3592–3602.

17 M. Shen, C. Ruan, Y. Chen, C. Jiang, K. Ai and L. Lu, *ACS Appl. Mater. Interfaces*, 2015, **7**, 1207–1218.

18 X. Ma, W. Zhang, Y. Deng, C. Zhong, W. Hu and X. Han, *Nanoscale*, 2018, **10**, 4816–4824.

19 N. Yao, T. Tan, F. Yang, G. Cheng and W. Luo, *Mater. Chem. Front.*, 2018, **2**, 1732–1738.

20 Y. Li, X. Fu, W. Zhu, J. Gong, J. Sun, D. Zhang and J. Wang, *Inorg. Chem. Front.*, 2019, **6**, 2090–2095.

21 Y. Yang, M. Yuan, H. Li, G. Sun and S. Ma, *Electrochim. Acta*, 2018, **281**, 198–207.

22 M. Zhu, Z. Zhang, H. Zhang, H. Zhang, X. Zhang, L. Zhang and S. Wang, *J. Colloid Interface Sci.*, 2018, **509**, 522–528.

23 B. Souvignier, H. Wondratschek, M. I. Aroyo, G. Chapuis and A. M. Glazer, 2016, pp. 42–74.

24 X. Zhu, J. Dai, L. Li, D. Zhao, Z. Wu, Z. Tang, L. J. Ma and S. Chen, *Carbon N. Y.*, 2020, **160**, 133–144.

25 L. Chen, L. Hu, C. Xu, L. Yang, W. Wang, J. Huang, M. Zhou and Z. Hou, *Carbon Lett.*, 2023, **33**, 2087–2094.

26 G. Wang, J. Chen, K. Li, J. Huang, Y. Huang, Y. Liu, X. Hu, B. Zhao, L. Yi, T. W. Jones and Z. Wen, *Nano Energy*, 2022, **92**, 106751.

27 G. Wu, X. Dong, J. Mao, G. Li, C. Zhu, S. Li, A. Chen, G. Feng, Y. Song, W. Chen and W. Wei, *Chem. Eng. J.*, 2023, **468**, 143640.

28 L. Li, Z. Zhang, H. Chen and F. Chen, *Nano Res.*, 2023, **16**, 4596–4602.

29 W. Luo, H. Tian, Q. Li, G. Meng, Z. Chang, C. Chen, R. Shen, X. Yu, L. Zhu, F. Kong, X. Cui and J. Shi, *Adv. Funct. Mater.*, 2024, **34**, 1–13.

30 Z. Gui, Y. Jia, X. Liao, T. Yan, B. Gao, W. Zhang, L. Chen, Q. Gao, Y. Zhang and Y. Tang, *Chem. Sci.*, 2024, **15**, 8145–8155.

31 Y. Song, X. Wan, Y. Miao, J. Li, Z. Ren, B. Jin, H. Zhou, Z. Li and M. Shao, *Appl. Catal. B Environ.*, 2023, **333**, 122808.

32 H. Yang, G. Vijaykumar, Z. Chen, J. N. Hausmann, I. Mondal, S. Ghosh, V. C. J. Nicolaus, K. Laun, I. Zebger, M. Driess and P. W. Menezes, *Adv. Funct. Mater.*, 2023, **33**, 2303702.

33 Y. Pei, Z. Pi, H. Zhong, J. Cheng and F. Jin, *J. Mater. Chem. A*, 2022, **10**, 1309–1319.

34 H. Yu, W. Wang, Q. Mao, K. Deng, Z. Wang, Y. Xu, X. Li, H. Wang and L. Wang, *Appl. Catal. B Environ.*, 2023, **330**, 122617.

35 J. Du, Y. Qin, T. Dou, J. Ge, Y. Wang, X. Zhao, F. Zhang and X. Lei, *ACS Appl. Nano Mater.*, 2022, **5**, 10174–10182.

36 J. Li, X. Meng, X. Song, J. Qi, F. Liu, X. Xiao, Y. Du, G. Xu, Z. Jiang, S. Ye, S. Huang and J. Qiu, *Adv. Funct. Mater.*, 2024, **2316718**, 1–14.

37 H. Wan, C. Dai, L. Jin, S. Luo, F. Meng, G. Chen, Y. Duan, C. Liu, Q. Xu, J. Lu and Z. J. Xu, *ACS Appl. Mater. Interfaces*, 2022, **14**, 14293–14301.

38 H. Yang, P. V. Menezes, G. Dai, G. Vijaykumar, Z. Chen, M. Al-Shakran, T. Jacob, M. Driess and P. W. Menezes, *Appl. Catal. B Environ.*, 2023, **324**, 122249.

39 T. Begildayeva, J. Theerthagiri, S. J. Lee, A. Min, G. Kim, S. Manickam and M. Y. Choi, *Energy Environ. Mater.*, 2024, **7**, 1–9.

40 J. Kim, T. Begildayeva, J. Theerthagiri, C. J. Moon, A. Min, S. J. Lee, G.-A. Kim and M. Y. Choi, *J. Energy Chem.*, 2023, **84**, 50–61.

41 N. Jiang, X. Liu, J. Dong, B. You, X. Liu and Y. Sun, *ChemNanoMat*, 2017, **3**, 491–495.

42 X. Zhang, M. Han, G. Liu, G. Wang, Y. Zhang, H. Zhang and H. Zhao, *Appl. Catal. B Environ.*, 2019, **244**, 899–908.

43 A. M. Román, J. C. Hasse, J. W. Medlin and A. Holewinski, *ACS Catal.*, 2019, **9**, 10305–10316.